J. Fluid Mech. (2000), *vol.* 415, *pp.* 117–153. Printed in the United Kingdom

Statistical mechanical description and modelling of turbulent collision of inertial particles

By LIAN-PING WANG†, ANTHONY S. WEXLER AND YONG ZHOU

Department of Mechanical Engineering, 126 Spencer Laboratory, University of Delaware, Newark, DE 19716-3140, USA
e-mail: lwang@me.udel.edu

(Received 20 August 1998 and in revised form 3 March 2000)

The collision rate of monodisperse solid particles in a turbulent gas is governed by a wide range of scales of motion in the flow. Recent studies have shown that large-scale energetic eddies are the dominant factor contributing to the relative velocity between two colliding particles (the turbulent transport effect), whereas small-scale dissipative eddies can enhance the collision rate significantly by inducing local non-uniform particle distribution (the accumulation effect). The turbulent transport effect is most noticeable when the particle inertial response time τ_p is of the order of the flow integral timescale and the accumulation effect is most pronounced when τ_p is comparable to the flow Kolmogorov time.

We study these two contributions separately through direct numerical simulations. The two effects are quantified carefully with a numerical procedure that is independent of the computation of average collision rate. This facilitates the study of not only the statistical description of the collision kernel, but also the relative contributions and modelling of the two physical effects. Simulations at several flow Reynolds numbers were performed to suggest a model for the accumulation effect. The data show that the accumulation effect scales linearly with flow Taylor microscale Reynolds number R_λ, while the theory for fully developed turbulence indicates that the maximum level of the turbulent transport effect scales with $R_\lambda^{1/2}$. Finally, an integrated model has been developed to predict the collision rate at arbitrary flow Reynolds numbers and particle inertia.

1. Introduction

Turbulent coagulation, the process of collision-induced merging of particles in a suspension of solid particles or liquid droplets, plays an important role in many natural and industrial processes. Early studies on this subject were motivated by the need to understand the growth of liquid droplets in turbulent clouds (e.g. Saffman & Turner 1956; Pruppacher & Klett 1978). Subsequent studies, especially addressing the effects of finite particle inertia, were directed to better model and control particle growth in industrial processes, such as droplet growth in wet steam generators (Williams & Crane 1979) and spray atomization process (O'Rourke & Bracco 1980), dust separation in cyclones (Abrahamson 1975), and TiO_2 production (Xiong & Pratsinis

† Author for correspondence: Department of Mechanical Engineering, 126 Spencer Laboratory.

1991). Coagulation of fuel droplets may lead to reduced evaporation and burning rates, resulting in incomplete combustion. Turbulent coagulation can also affect pollutant formation and control (e.g. Flagan & Seinfeld 1988). Smoke ageing (i.e. the increase of particle size in smoke) is a result of particle coagulation, which alters the dispersion and transport of turbulent flames, reduces the rate of smoke particle burn-out, and increases particulate emission (Delichatsios 1980).

The overall coagulation rate of finite-size particles in fluid turbulence is governed by three consecutive and interrelated processes: (i) geometric collision due to particle–turbulence interactions and Brownian diffusion (Saffman & Turner 1956; Abrahamson 1975; Williams & Crane 1983; Hu & Mei 1997; Kruis & Kusters 1997; Sundaram & Collins 1997; Wang, Wexler & Zhou 1998*a*; Zhou, Wexler & Wang 1998), (ii) collision efficiency due to local particle–particle aerodynamic interactions (e.g. Jonas & Goldsmith 1972; Delichatsios 1980; Koziol & Leighton 1996; Brunk, Koch & Lion 1997, 1998*a*, *b*), and (iii) coagulation efficiency as determined by surface sticking characteristics (such as van der Waals forces, particle wetness, and electrostatic charges, e.g. Delichatsios 1980; Zinchenko & Davis 1995; Brunk *et al.* 1997). Here, we consider only the geometric collision rates of finite-inertia particles. The objective is to determine the average geometric collision rate of finite-inertia, monodisperse, heavy particles as a function of turbulence characteristics and particle inertial response time τ_p. A description of the average collision rate is required for modelling the particle size distribution in turbulent suspension using population balance equations.

In their pioneer work on geometric collision rates in a turbulent suspension, Saffman & Turner (1956) presented the first accurate formulation of the geometric collision kernel for zero-inertia particles based on the collision sphere concept. Recently, we revisited this spherical formulation (Wang *et al.* 1998*a*, *b*). Specifically, we clarified all the assumptions underlying this spherical formulation (Wang *et al.* 1998*a*) and showed that, rigorously speaking, finite corrections may be needed when the formulation is applied to the modelling of real coagulation processes. Saffman & Turner (1956) also provided an approximate formulation based on the concept of collision cylinder (the cylindrical formulation). Whereas both the spherical and cylindrical formulations (details are given in § 2) have been used for over 40 years, we were able to show, for the first time, that the spherical formulation is the more accurate model for the turbulent collision kernel of zero-inertia particles (Wang *et al.* 1998*b*). The first objective of this paper is to compare these two formulations when they are extended to finite-inertia particles.

Since the work of Saffman & Turner (1956), several studies have been undertaken to extend their results to finite-inertia particles. These include Panchev (1971) for the case of τ_p spanning τ_k, Williams & Crane (1983) for intermediate-inertia particles with $\tau_k < \tau_p < T_e$, and Abrahamson (1975) for very large particles with $\tau_p > T_e$, where τ_k is the flow Kolmogorov time and T_e is the flow integral timescale. Yuu (1984) and Kruis & Kusters (1997) considered the combined effect of local shear and unequal inertial response times on the collision rate for arbitrary τ_p. All the above were carried out within the framework of a stochastic theory of turbulence under the assumption that the particle concentration field is uniform. The key in these stochastic theories is to identify the proper range of scales of motion in the fluid turbulence which contribute most actively to the relative velocity between two colliding particles. In these studies, closure assumption of one type or another was usually assumed in order to derive an expression for the average particle relative velocity. The contribution of the relative velocity to the collision kernel will be termed *the turbulent transport effect* in this paper. The turbulent transport effect is most important when τ_p is of the order of T_e (Sundaram & Collins 1997; Zhou *et al.* 1998).

A recent discovery in fully developed, turbulent particle-laden flows is preferential particle concentration – the fact that intense vortex tube structures, which characterize the dissipation-range dynamics in fully developed turbulence, can lead to a very non-uniform particle concentration field. The preferential concentration in turbulence was first illustrated by Maxey (1987) then demonstrated by Squires & Eaton (1991) and Wang & Maxey (1993) through direct numerical simulations. It has also been observed experimentally by Fessler, Kulick & Eaton (1994). The preferential concentration was found to follow a Kolmogorov scaling, namely, being most effective in producing a non-uniform concentration when $\tau_p/\tau_k \sim 1$ (Wang & Maxey 1993). Since the local collision rate is proportional to the square of the local concentration in a monodisperse suspension, the preferential concentration must have a significant effect on the average collision kernel. We shall term the additional increase in the average collision kernel solely due to the non-uniform particle concentration *the accumulation effect*. Several recent numerical studies have indeed demonstrated that this accumulation effect can cause a significant increase in the collision kernel at low- to moderate-flow Reynolds numbers (Sundaram & Collins 1997; Zhou *et al.* 1998). A first theoretical formulation of the collision kernel which includes the accumulation effect was given recently by Sundaram & Collins (1997) in terms of the radial distribution function at contact. An asymptotic theory for the accumulation effect has been developed for $\tau_p < \tau_k$ in terms of the moments of local particle concentration by Zhou *et al.* (1998).

The second objective of this paper is to separate out numerically the relative contributions of the turbulent transport effect and the accumulation effect. We will present the numerical procedure which allows separate quantifications of these two effects. Together with an independent numerical quantification of the net collision kernel, we can not only compare the spherical and cylindrical formulations, but also suggest models for the two physical effects and the net collision kernel.

There have been only a few physical experiments designed to measure the collision rate in a turbulent suspension (Kuboi, Komasawa & Otake 1972; Delichatsios & Probstein 1974; Higashitani *et al.* 1983; de Boer, Hoedemakers & Thoenes 1989; Lichtenfeld *et al.* 1995). These experiments have provided valuable information to compare with theoretical models. However, such comparison is very limited and may be misleading since (i) most theories address only a single collision mechanism and (ii) it is difficult to perform well-controlled experiments in which one can isolate one collision mechanism from others (say, shear-induced collision from Brownian coagulation, geometric collision from hydrodynamic interactions). Such a lack of well-controlled experiments on the turbulent coagulation process makes numerical simulation a valuable tool, as has been shown previously (Hu & Mei 1997; Sundaram & Collins 1997; Zhou *et al.* 1998). In our numerical experiments, we make use of turbulent flow fields generated by numerically integrating the full Navier–Stokes equations directly. This is known as direct numerical simulations (DNS) of turbulence. By this means, local flow dynamic features are represented without any *ad hoc* modelling.

The paper is organized as follows. In the next section we modify the recent theoretical formulation of Sundaram & Collins (1997) in view of our recent observation (Wang *et al.* 1998*b*) regarding the comparison of the spherical and cylindrical formulations. We shall also state all major assumptions that need to be examined in our numerical experiments. A description of the numerical methods is presented in § 3. In § 4 we discuss the numerical results thoroughly. In the light of numerical results, we then propose empirical models for the collision statistics in § 5. Finally, the main conclusions are drawn in § 6.

2. Theory

2.1. *Statistical description of collision kernel*

In general the collision statistics in a mono-disperse particle assembly can depend on τ_p/τ_k, carrier flow characteristics especially flow Reynolds number R_λ, particle size, and particle volumetric loading. We focus here on the effects of τ_p/τ_k and R_λ. The particle diameter is assumed to be comparable or less than the Kolmogorov microscale of turbulence, namely, $d_p \leqslant \eta$. We have shown in Wang *et al.* (1998*a*) that the linear expansion result for relative velocity statistics at $d_p \ll \eta$ actually applies to $d_p \leqslant \eta$. This is not surprising when we recognize that the average radius of small-scale vortices is about 4η (Jimenez *et al.* 1993), which implies that across the lengthscale of η the local velocity gradients remain uniform. However, even for $R < \eta$, the accumulation effect may depend on the particle size, since the smallest lengthscale of the particle concentration field scales with R not η. Without considering local particle–particle hydrodynamic interactions, particles may accumulate indefinitely around a vortex structure, leading to small-scale features in the particle concentration fields at scales less than η. This may cause a strong dependence of the accumulation effect on the particle size, as demonstrated recently by Reade & Collins (1998). It is reasonable to expect that this size dependence would saturate when the local particle–particle hydrodynamic interactions are considered.

Another parameter not considered in this work is the particle volumetric loading. The volumetric loading can affect the collision statistics in at least two ways. First, if the volumetric loading is not small so that the mass loading is sufficient to modify the carrier flow, the geometric collision rates will be affected. Secondly, even if the flow modulation can be neglected, the physical non-overlapping requirement of the particle assembly can lead to dependence of the collision rate on the volume fraction, as shown in Wang *et al.* (1998*a*). In this work, particle volume fraction and mass loading are assumed to be sufficiently low so that the gas turbulence is not significantly affected by the presence of particles. This assumption may be questionable even in dilute flows owing to preferential concentration. An upper limit for the particle volume fraction commonly cited for one-way coupling is 10^{-6} (Elghobashi 1994), which may be taken as the limiting condition for the analysis to be developed in this paper. Since we neglect flow modulation and as the non-overlapping correction (Wang *et al.* 1998*a*) is usually small, we do not explicitly consider the volumetric loading as a parameter here. Under the one-way coupling assumption, the collision rate is linearly proportional to the number of interacting pairs in the particle assembly. We will take advantage of this linear dependence by allowing the particle volume fraction to be of the order of 10^{-3} in order to have a sufficiently large number of collision events. This will produce accurate numerical results since the statistical uncertainty of the numerical collision kernel decreases with the number of particles in the system (e.g. Wang *et al.* 1998*a*).

Another simplification is that the gravitational (or body force) effect is not included. This assumption is made to allow us to focus on the effect of particle inertia and interphase drag, as in other related studies (Abrahamson 1975; Williams & Crane 1983; Sundaram & Collins 1997). Although the description of gravitational collision alone is well established, our understanding of the couplings between the particle inertia and settling on particle–particle collisions remains incomplete (Reuter, de Villiers & Yavin 1988; Wang & Maxey 1993; Pinsky & Khain 1994; Khain & Pinsky 1995).

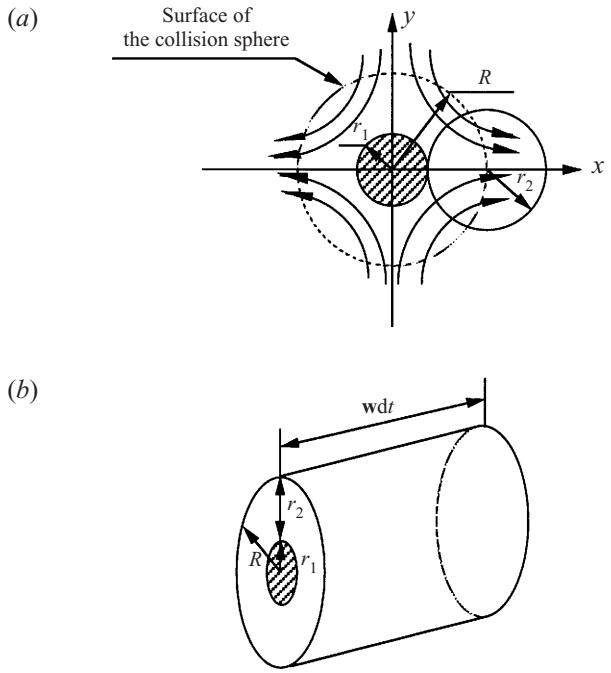

FIGURE 1. Geometrical description of the two statistical formulations. (*a*) Projection of the collision sphere on the (*x*, *y*)-plane. (*b*) The concept of the collision cylinder.

In a monodisperse system consisting of N_p particles in a volume Ω, the collision rate per unit volume, $\dot{\mathcal{N}}_c$, is given by

$$\dot{\mathcal{N}}_c = \Gamma \frac{n_0^2}{2}, \tag{2.1}$$

provided that $N_p \gg 1$, where $n_0 \equiv N_p/\Omega$ is the average particle number concentration in the volume and Γ is the average collision kernel.

We shall first review the statistical mechanical description of Γ for zero-inertia particles (i.e. $\tau_p = 0$) as it is now well established (Saffman & Turner 1956; Wang *et al.* 1998*a*, *b*). There are two commonly used formulations known as the spherical formulation and the cylindrical formulation. In the spherical formulation, Γ is described as the average volume of fresh fluid entering a collision sphere per unit time,

$$\Gamma^{sph} = 2\pi R^2 \langle |w_r| \rangle. \tag{2.2}$$

The collision sphere is defined, relative to a reference particle, as a sphere of radius $R = d_p$, centred on the reference particle (figure 1*a*). Here, d_p is the diameter of the particles, w_r is the radial component of the relative velocity $\boldsymbol{w}$, namely, $w_r = \boldsymbol{w} \cdot \boldsymbol{R}/R$, $\boldsymbol{R}$ is the separation vector, and $R \equiv |\boldsymbol{R}|$. One important assumption of (2.2) is that the relative velocity $\boldsymbol{w}$ is incompressible, thus influx and outflux over the sphere surface are equal. The collision kernel is then half the surface area multiplied by the average magnitude of the radial relative velocity.

In the cylindrical formulation, Γ is described in terms of the relative velocity directly and is defined as the cylindrical volume passing through a reference particle per unit time, with cross-sectional area πR^2 and length $|\boldsymbol{w}|$ (figure 1*b*). The average

collision kernel is then

$$\Gamma^{cyl} = \pi R^2 \langle |\boldsymbol{w}| \rangle. \tag{2.3}$$

In both formulations, the angle brackets denote averages over all orientations of $\boldsymbol{R}$, space, and the time interval of numerical simulations in stationary, isotropic turbulence.

Recently, we have shown that the spherical formulation is more appropriate than the cylindrical formulation for turbulent coagulation (Wang *et al.* 1998*b*). For zero-inertia particles, the spherical formulation gives an accurate prediction for Γ, while the cylindrical formulation can overpredict Γ by 20% or more in a turbulent flow field.

The first theoretical description of Γ for finite-inertia particles was developed by Sundaram & Collins (1997). They considered both the turbulent transport effect and the accumulation effect on Γ and derived an expression for the collision kernel as

$$\Gamma^{cyl} = \pi R^2 \langle |\boldsymbol{w}| \rangle g(R), \tag{2.4}$$

where the additional part $g(R)$, is known in statistical mechanics as the radial distribution function at contact. This measures the level of particle pair accumulation with interparticle distance of R and as such represents directly the accumulation effect. The term $g(R)$ is defined as the probability density of observing a particle pair at contact in the actual suspension, normalized by the corresponding value in a nominally uniform suspension. In the limit of weak inertia ($\tau_p \to 0$), this formulation is identical to the cylindrical formulation (2.3). This results from an underlying assumption in Sundaram & Collins (1997) that the probability density function of $\boldsymbol{w}$ is independent of the orientation of $\boldsymbol{R}$.

In view of the above discussion on the comparison of the two formulations for zero-inertia particles, a more accurate formulation based on the spherical formulation is suggested here

$$\Gamma^{sph} = 2\pi R^2 \langle |w_r| \rangle g(R). \tag{2.5}$$

There is, however, one major assumption involved in (2.5): the net radial relative inward flux is the same as the net radial relative outward flux – we shall call this the flux-balance assumption. This assumption will be examined in our numerical simulations. Except for the above-mentioned assumption, equation (2.5) is expected to be accurate for predicting the collision kernel of finite-inertial particles. The complexity in modelling the collision kernel for arbitrary particle inertia could be greatly reduced by considering the turbulent transport effect and the accumulation effect separately using (2.5).

The flux-balance assumption should be valid for a truly stationary suspension. Suppose in a numerical simulation, particles are randomly distributed in the flow at $t = 0$. The interactions of particles with vortical structures will accumulate particles in local regions while the advection by large-scale flows tends to counteract the accumulation. Once a balance between the two processes is established, the accumulation level becomes stationary. The question is then how long one has to wait before this stationarity is reached. Wang & Maxey (1993) computed global accumulation measures after the particles were introduced into the flow and suggested that stationarity was almost established after $t = 2T_e$.

If true stationarity is not reached, the transient effect can be taken into account as follows. Let P be the probability of observing $w_r < 0$, w_r^- is the average magnitude of negative radial relative velocity, w_r^+ is the average magnitude of positive radial relative velocity. The correct collision kernel Γ_c, according to the original spirit of

Saffman & Turner (1956), should be

$$\Gamma_c = 4\pi R^2 P\, w_r^- g(R). \tag{2.6}$$

We note that

$$\langle |w_r| \rangle = P\, w_r^- + (1-P) w_r^+, \tag{2.7}$$

therefore,

$$\Gamma_c = \Gamma^{sph} \times \frac{2C_p}{1+C_p}, \quad \text{with} \quad C_p \equiv \frac{P\, w_r^-}{(1-P) w_r^+}, \tag{2.8}$$

where C_p represents the ratio of net inward flux to net outward flux. During the transient stage, the level of local particle accumulation has not saturated, thus the net inward flux is larger than the net outward flux, giving $C_p > 1$. As a result, the spherical formulation (2.5) can underpredict the collision kernel slightly. This will be shown in § 4.

Finally, we note that the flux-balance assumption differs from the incompressibility assumption of the particle velocity field. It is known that the local particle velocity field is compressible (Maxey 1987) even when the accumulation level is stationary. Roughly speaking, the ratio of w_r^-/w_r^+ can be viewed as a measure of the compressibility in the particle velocity field. This quantity will be discussed in our numerical experiments in § 4.

2.2. *Description of* $\langle |w_r| \rangle$ *and the eddy–particle interaction model*

In Zhou *et al.* (1998), we proposed a simple one-dimensional, eddy–particle interaction model to predict the turbulent transport effect. In that model, the motion of particles is treated as a succession of interactions with turbulent eddies of constant eddy lifetime. The eddy velocity is random with standard deviation equal to the r.m.s. fluid fluctuation velocity u'. A brief description of the model results is repeated here for the purposes of later comparison with simulation results and for introducing necessary notation.

Let $v_r^{(1)}$ and $v_r^{(2)}$ be the radial velocities of the two particles at collision. Assuming the relative velocity $w_r \equiv v_r^{(2)} - v_r^{(1)}$ between two colliding particles follows a Gaussian distribution with a standard deviation σ_w, then $\langle |w_r| \rangle = (2/\pi)^{1/2} \sigma_w$. While σ_w, according to the definition, can be expressed as

$$\sigma_w = (\langle w_r^2 \rangle)^{1/2} = [2(v_p')^2 - 2\langle v_r^{(1)} v_r^{(2)} \rangle]^{1/2}, \tag{2.9}$$

where v_p' denotes the r.m.s. particle fluctuation velocity. The eddy–particle interaction model gives (Zhou *et al.* 1998)

$$\frac{(v_p')^2}{u'^2} = 1 - \theta[1 - \exp(-1/\theta)], \tag{2.10}$$

where $\theta = 0.5\tau_p/T_e$. The particle velocity correlation coefficient is determined by the interactions of the two particles with the same eddy. Assuming two colliding particles enter the eddy at a same time but may collide at any time during the eddy lifetime, we found that the particle velocity correlation coefficient, ρ_{12}, can be expressed as

$$\rho_{12} \equiv \frac{\langle v_r^{(1)} v_r^{(2)} \rangle}{u'^2} = 1 - \frac{\theta}{2} \frac{[1 - \exp(-1/\theta)]^2}{\{1 - \theta[1 - \exp(-1/\theta)]\}}. \tag{2.11}$$

Putting the above together, we have

$$\frac{\langle |w_r| \rangle}{u'} = \left(\frac{2\theta}{\pi}\right)\left[1 - \exp\left(-\frac{1}{\theta}\right)\right], \tag{2.12}$$

which has a maximum of $\langle |w_r| \rangle = 0.509u'$ at $\theta = 0.796$, or $\tau_p/T_e = 1.59$. This model will be compared with numerical results in § 4.

3. Numerical experiment

We consider the collision statistics in a dilute suspension of solid particles in a turbulent gas. The numerical methods for turbulent-flow simulations and particle-collision detection follow from our previous studies (Wang & Maxey 1993; Wang *et al.* 1998*a*; Zhou *et al.* 1998). Therefore, only a brief description of the methods is given, along with statistics of the numerical flow fields. The numerical methods for quantifying separately the turbulent transport and accumulation effects will be reported for the first time, and therefore, they will be described in detail, along with validation procedures.

3.1. *Flow field*

A homogeneous and isotropic turbulent flow was generated by full numerical simulations using a pseudo-spectral method. The incompressible Navier–Stokes equations

$$\frac{\partial \boldsymbol{u}}{\partial t} = \boldsymbol{u} \times \boldsymbol{\omega} - \nabla\left(\frac{P}{\rho} + \frac{1}{2}\boldsymbol{u}^2\right) + \nu\nabla^2\boldsymbol{u} + \boldsymbol{f}(\boldsymbol{x}, t), \tag{3.1}$$

were solved along with the continuity equation $\nabla \cdot \boldsymbol{u} = 0$ in a periodic box of side 2π. Here, $\boldsymbol{\omega} \equiv \nabla \times \boldsymbol{u}$ is the vorticity, P is the pressure. The flow was generated from rest by the random forcing term $\boldsymbol{f}(\boldsymbol{x}, t)$ which is non-zero only at low wavenumbers, $|\boldsymbol{k}| < 8^{1/2}$.

In this paper, the flow was frozen after the statistically stationary stage was reached, and particles were then introduced into the flow. The start of particle release will be denoted as $t = 0$. This provides us with an identical flow microstructure for different runs with various particle parameters, which limits statistical fluctuations and speeds data collection. Since the particle trajectories are chaotic even in these complex frozen flows, each particle interacts with many turbulent eddies in the flow. The fact that these eddies have infinite lifetime leads to overprediction of the level of the accumulation effect (see, e.g. Zhou *et al.* 1998), and possibly even the level of turbulent transport effect is somewhat over estimated. However, the qualitative features reported here should be the same as in evolving flows, as shown in our recent work for $\tau_p/\tau_k = O(1)$ (Zhou *et al.* 1998). Sundaram & Collins (1997) have reported more results on the evolving flow case. As will be shown later in the paper, our results agree well with those of Sundaram & Collins (1997). More thorough studies on the bounds of the unsteady effects are given by Brunk *et al.* (1998*a*), using random Fourier modes representations.

Table 1 lists the flow parameters (from top to bottom): the component r.m.s. fluctuating velocity u', average dissipation rate $\bar{\epsilon}$, and kinematic viscosity ν are the primary parameters which control the scales of the flow. The Taylor microscale Reynolds number is defined as $R_\lambda \equiv u'\lambda/\nu$, where λ is the transverse Taylor microscale $\lambda \equiv u'/\langle(\partial u_1/\partial x_1)^2\rangle^{1/2} = (15\nu u'^2/\bar{\epsilon})^{1/2}$. Other derived flow scales are Kolmogorov length $\eta \equiv (\nu^3/\bar{\epsilon})^{1/4}$, timescale $\tau_k \equiv (\nu/\bar{\epsilon})^{1/2}$, large-eddy turnover time $T_e \equiv u'^2/\bar{\epsilon}$, and the timescale ratio T_e/τ_k. Parameters of the particulate phase are the collision radius

Grid resolution	32^3	64^3	96^3	128^3
u'	17.02	18.22	18.30	18.64
$\bar{\epsilon}$	3568.8	3421.0	3554.7	3374.4
ν	0.6000	0.2381	0.1387	0.09450
R_λ	24.25	45.05	58.41	75.36
η	0.08820	0.04457	0.02943	0.02236
τ_k	0.01297	0.008343	0.006247	0.005292
T_e	0.08117	0.09704	0.09421	0.1030
T_e/τ_k	6.26	11.6	15.1	19.5
R/η	1.0	1.0	1.0	1.0
N_p	3072×2	8192	5280×2	6144×2
α ($\times 10^3$)	8.9	1.5	0.57	0.29

TABLE 1. Flow characteristics and parameters for the particle system.

R (which is equal to the particle diameter for a monodisperse system), total number of particles N_p, and particle volume fraction α. Other details of the simulated flows can be found in Wang & Maxey (1993).

3.2. *Particle motion*

We consider the motion of small, heavy, spherical particles in a non-uniform turbulent flow. Under the assumption that the density of the particle ρ_p is much larger than the density of the fluid ρ, and that a quasi-steady Stokes drag can be used, the equation of motion for a heavy particle becomes (Maxey & Riley 1983)

$$\frac{\mathrm{d}\boldsymbol{V}(t)}{\mathrm{d}t} = \frac{\boldsymbol{u}(\boldsymbol{Y}(t), t) - \boldsymbol{V}(t)}{\tau_p}, \tag{3.2}$$

where $\boldsymbol{V}(t)$ and $\boldsymbol{Y}(t)$ are the velocity and the centre position of a heavy particle, respectively. $\tau_p = \rho_p d_p^2/(18\rho\nu)$ is the particle inertial response time. Here, d_p and ρ_p are particle diameter and density; ρ is fluid density.

Typically, $10^3 \sim 10^4$ particles were introduced at $t = 0$ into the computational domain at random initial positions with an initial velocity equal to the local fluid velocity. After about $3\tau_p$, any effects of the initial velocity condition on the particle motion became lost. The simulation was continued for at least $13\tau_p$ or 5 large-eddy turnover times during which collision counts and other statistical averages were taken. It should be noted that the particle concentration field may not reach its asymptotic, statistically stationary stage at $t = 3\tau_p$ since the local accumulation process is affected by large-scale fluid motion (Wang & Maxey 1993). On the other hand, in practical applications, the particle collision statistics shortly after the particle release may be of more interest than the asymptotic value. With this in mind and for the purpose of obtaining a small statistical uncertainty, we take $t = 3\tau_p$ as the starting time for all statistical averages. The particle concentration field for $\tau_p/\tau_k = O(1)$ may not reach the statistically stationary stage completely, as will be shown by a slight unbalance of relative fluxes in § 4. This transient effect can be corrected through (2.8).

3.3. *Collision rate $\dot{\mathcal{N}}_c$ and the DNS collision kernel*

The collision detection algorithm used to compute $\dot{\mathcal{N}}_c$ was described in our recent papers (Wang *et al.* 1998*a*; Zhou *et al.* 1998) and will not be repeated here.

For convenience, we refer to the collision kernel computed directly based on the

numerical value of $\dot{\mathscr{N}}_c$ and (2.1) as the DNS collision kernel

$$\Gamma_{DNS} = 2\dot{\mathscr{N}}_c / n_0^2. \tag{3.3}$$

In this paper, we used Scheme 1 as described in Zhou *et al.* (1998) to compute $\dot{\mathscr{N}}_c$. In this scheme, particles were allowed to overlap in the system at the beginning of a timestep and were not removed from the system after collision. This was shown to be the only scheme that is consistent with the Saffman & Turner (1956) formulation. Use of this scheme will facilitate the validation procedure for independent, separate quantifications of the turbulent transport effect and the local accumulation effect (see § 3.4). Another advantage of using this scheme is that we can calculate the radial distribution function at contact $g(R)$ accurately. In contrast, in the hard-sphere model used by Sundaram & Collins (1997), $g(R)$ cannot be determined directly, so a local extrapolation was employed. For the purpose of examining the two statistical formulations, an accurate evaluation of $g(R)$ is essential.

We consider only binary collisions as the particle loadings are dilute enough in our numerical simulations (see table 1). The collision search was conducted using the efficient cell-index method and the concept of linked lists (Allen & Tildesley 1987). The collision-detection cell was made large enough so that two particles residing in unconnected cells would not collide within a numerical timestep (Sundaram & Collins 1996; Wang *et al.* 1998*a*). Averages over both time and initial realizations of particle locations were used to reduce the statistical uncertainties.

3.4. *Relative velocities and* $g(R)$

The Lagrangian pair relative velocity statistics ($\langle |w_r| \rangle$ or $\langle |\boldsymbol{w}| \rangle$) measures the turbulent transport effect while the radial distribution function at contact $g(R)$ quantifies the accumulation effect. Their computations were completely independent of the collision kernel simulation. The procedure for relative velocities and $g(R)$ calculations is as follows:

(i) *Particle pair identification*: at each timestep, we detected all the pairs with interparticle distance r given as $R-\delta/2 < r < R+\delta/2$ with $\delta = 2\%R$. This detection was performed using the same efficient cell-index method and the concept of linked lists. However, the size of the detection grid, W, could now be made much smaller than that needed for the collision kernel simulation. In fact, $W = R+\delta/2$ is sufficient for the detection. Obviously, only a fraction of these pairs will participate in collision events during the next numerical timestep. A question arises as to how large we should set δ/R. The smaller the δ/R, the more precise the pair is closer to contact. On the other hand, δ/R should be made large enough so that there are enough independent samples. As long as $\delta/R \ll 1$, the relative velocity statistics should not depend on δ/R. This is demonstrated in figure 2, which shows $\langle |w_r| \rangle$ and $g(R)$ as a function of δ/R. The error bars represent the statistical standard deviations computed based on 12 realizations. We observe that $\langle |w_r| \rangle$ and $g(R)$ are insensitive to the thickness of the spherical shell for $\delta/R < 0.2$. We typically used $\delta = 2\%R$. For larger shell thickness, $\langle |w_r| \rangle$ increases with δ because a slightly larger size range of eddies of larger velocity fluctuations contributes to the relative velocity. On the other hand, the averaging over a larger shell reduces the level of non-uniform concentration, leading to a smaller $g(R)$.

(ii) $g(R)$, $\langle |w_r| \rangle$ *and* $\langle |\boldsymbol{w}| \rangle$ *calculation*: the simulation was run for the same period of time as in the collision kernel computation and the initial $3\tau_p$ time interval was not used for statistical averaging. The timestep $\mathrm{d}t$ can be made as large as possible as long as the particle trajectories can be integrated accurately, whereas in the collision kernel simulation, single collision among pairs may impose further restriction on the

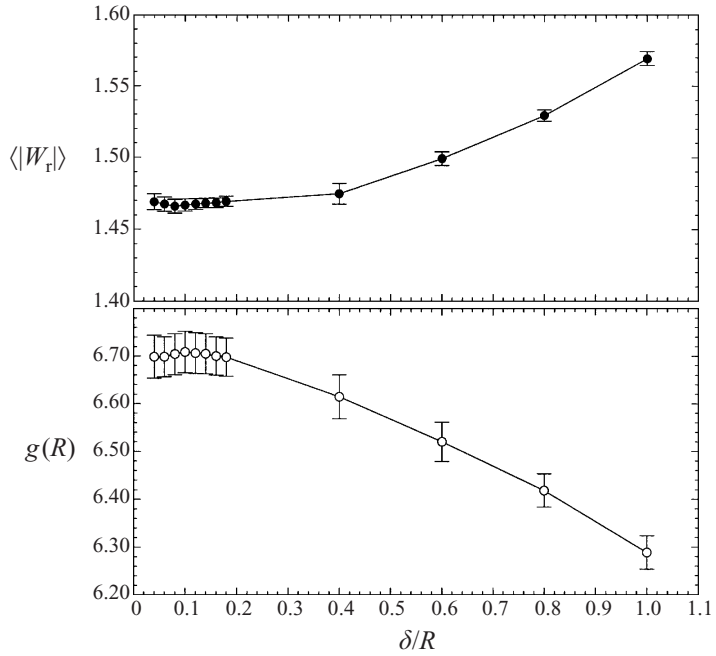

FIGURE 2. The dependence of $\langle |w_r| \rangle$ and $g(R)$ on δ, the thickness of the spherical shell. The test was carried out for $R_\lambda = 45$, $\tau_p/\tau_k = 0.9$, $R = \eta$, and total time interval $\Delta T = 0.5$ and $N_r = 12$.

step size. The rule of thumb was that $\mathrm{d}t = \min(0.2\tau_p, 0.2\tau_k)$. All the pairs of separation $R - \delta/2 < r < R + \delta/2$, along with individual particle velocities and the separation vectors, were recorded during the simulation. These data were postprocessed to give an average value for $|w_r|$ and $g(R)$ for that run. For example, $g(R)$ was computed simply as

$$g(R) = \frac{\text{Total number of pairs detected} \times V_{box}}{V_s \times N_t \times N_p(N_p - 1)/2}, \tag{3.4}$$

where $V_s = 4\pi[(R + \delta/2)^3 - (R - \delta/2)^3]/3$ is the shell volume, $V_{box} = (2\pi)^3$ is the volume of the flow domain, and N_t is the number of timesteps for which the pair detections were undertaken.

(iii) *Improving the statistics*: the simulation was repeated for N_r times with independent realizations of the initial particle locations, as in the collision kernel simulation. This then allows a further averaging over the realizations (thus further reducing the uncertainties) and, more importantly, an estimation of statistical uncertainties can be made. Note that the records in a given realization may not be independent when dt is small. But the averaged values over time from different realizations can be treated as independent samples.

To validate the above numerical procedure and the computer code, we first consider the case of fluid elements. In this case, the statistics of relative velocities between two Lagrangian particles are identical to those of relative velocities between two spatial points separated by the same distance. The two-point relative velocities can be computed easily based on the Eulerian fluid velocity field. For example, the resulting two-point relative velocity statistics for the $R_\lambda = 24$ flow field with $R = 0.8\Delta x$ are shown in the first row in table 2, while the relative velocity statistics based on all Lagrangian particle pairs are shown in the second row. Here, $\Delta x = 2\pi/N$ is the grid

Relative velocities	$\langle \lvert w_r \rvert \rangle$	$\langle w_r^2 \rangle$	$\langle \lvert \boldsymbol{w} \rvert \rangle$	$\langle \boldsymbol{w}^2 \rangle$
Eulerian two-point (E)	2.379	9.453	6.031	47.49
All Lagrangian pairs (L)	2.411±0.023	9.563	6.023±0.046	47.42
Colliding pairs only (c)	4.450±0.034	26.80	8.006±0.056	79.95

TABLE 2. Relative velocity statistics and their standard deviations for $R_\lambda = 24$, $R = 0.8\Delta x$, $N_p = 1024$, and $N_r = 21$.

spacing, where N is the mesh resolution. Table 2 shows that the relative velocity statistics for Lagrangian pairs are the same (within statistical uncertainties) as the Eulerian statistics, confirming our numerical procedure. One can confirm immediately that the spherical formulation is correct since $\Gamma^{sph} = 2\pi R^2 \langle |w_r|_L \rangle = 0.3738 \pm 0.0034$ while the collision kernel based on direct collision detection is $\Gamma^{DNS} = 0.3737 \pm 0.00036$. This consistency was pointed out in Wang *et al.* (1998*b*). On the other hand, the cylindrical formulation overestimates the collision kernel by about 25%.

It is important to note that the relative velocity statistics based on only those particle pairs which participate in collision events are quite different (last row in table 2). An explanation for this observation is given here. The main idea is that, even for uniform particle distribution, the non-uniform flow field leads to a non-uniform local distribution of the collision rate and thus the local number of samples being used for the computation of the average Lagrangian relative velocity between colliding pairs. Namely, the relative radial velocity between only colliding pairs can be related to those based on all pairs close to contact as

$$\begin{aligned}
\langle |w_r|_c \rangle &= \frac{\displaystyle\int |w_r| \times \text{ number of collision pairs per unit volume} \, \mathrm{d}^3\boldsymbol{x}}{\displaystyle\int \text{number of collision pairs per unit volume} \, \mathrm{d}^3\boldsymbol{x}} \\
&\approx \frac{\displaystyle\int |w_r| 2\pi R^2 |w_r| \mathrm{d}^3\boldsymbol{x}}{\displaystyle\int 2\pi R^2 |w_r| \mathrm{d}^3\boldsymbol{x}} \\
&= \frac{\displaystyle\int |w_r|^2 p(w_r) \mathrm{d}w_r}{\displaystyle\int |w_r| p(w_r) \mathrm{d}w_r} \\
&= \frac{\langle w_r^2 \rangle}{\langle |w_r| \rangle}. \qquad (3.5)
\end{aligned}$$

Here, the subscript c denotes statistics for colliding pairs only. A uniform concentration is assumed in the above derivation. For a Gaussian velocity field, we can show that (Wang *et al.* 1998*b*),

$$\langle |w_r|_c \rangle = \frac{\langle w_r^2 \rangle}{\langle |w_r| \rangle} = 1.5707 \langle |w_r| \rangle, \qquad (3.6)$$

namely, $\langle |w_r|_c \rangle$ must be larger than $\langle |w_r| \rangle$. For our DNS flow field, we find that $\langle |w_r|_c \rangle = 1.84 \langle |w_r| \rangle$, slightly larger than the estimation based on Gaussian fields.

In summary, the collision kernel measures dynamical events which are related to the

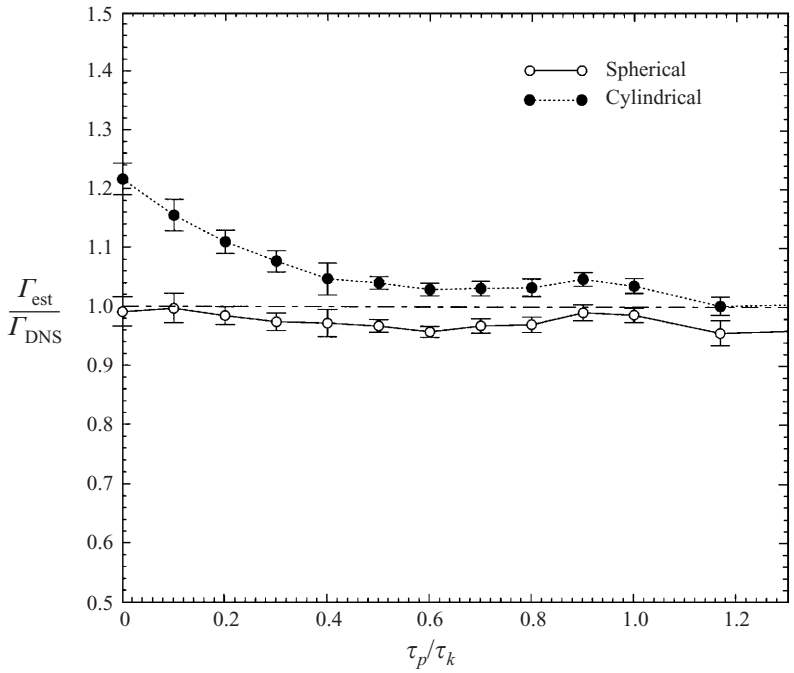

FIGURE 3. Comparison of the spherical and cylindrical formulations with DNS results for $\tau_p/\tau_k < 1.2$. The flow Reynolds number is 45.

change of inter-particle distance, while both relative velocities and $g(R)$ are kinematic quantities which are defined at any given time. In numerical simulations, since the timestep size is finite, the dynamic and kinematic properties must be computed separately. In a theoretical formulation, the limit of very small timestep can be taken, so a relationship between dynamic and kinematic properties can be established, as was demonstrated in the elegant analysis by Sundaram & Collins (1997).

For the purpose of presenting results in subsequent discussions, we denote the collision kernels estimated with numerical kinematic properties of the suspension using (2.4) and (2.5) as

$$\Gamma_{est}^{cyl} = \pi R^2 \langle |\boldsymbol{w}| \rangle g(R), \tag{3.7}$$

$$\Gamma_{est}^{sph} = 2\pi R^2 \langle |w_r| \rangle g(R). \tag{3.8}$$

4. Results

4.1. *Comparison between cylindrical and spherical estimations*

First, let us compare the cylindrical and spherical estimations with DNS results. Figure 3 shows the ratios of the estimated collision kernels, (3.7) and (3.8), over Γ_{DNS} as a function of particle Stokes number τ_p/τ_k at $R_\lambda = 45$. The error bars throughout this paper represent an estimation of standard deviations. A ratio of one implies that the estimate is exact. In agreement with Wang *et al.* (1998*b*), in the limit of $\tau_p/\tau_k \to 0$, the spherical formulation is exact, while the cylindrical formulation overpredicts the collision kernel by 22%. The interesting observation is that the difference between the two formulations diminishes very quickly as τ_p/τ_k increases. This can be explained

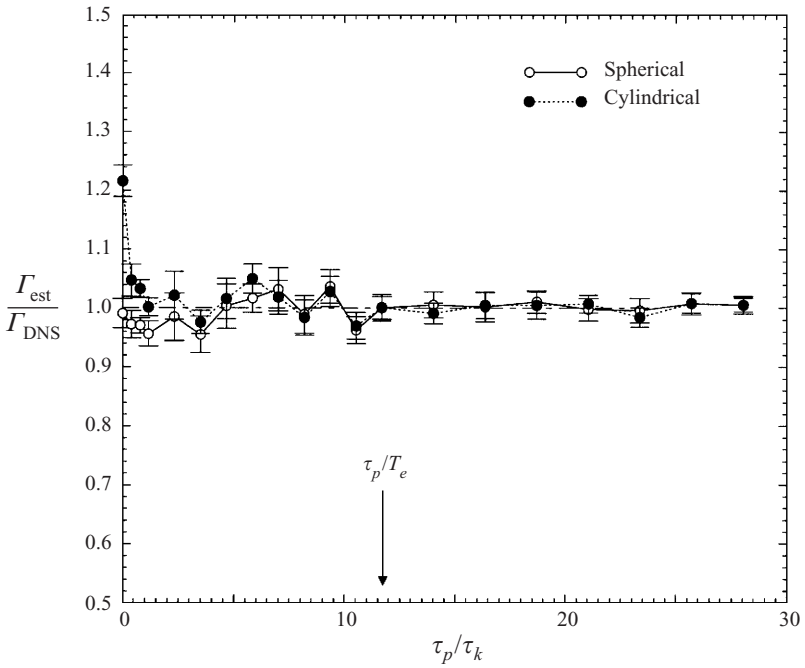

FIGURE 4. Comparison of the spherical and cylindrical formulations for a much wider range of particle inertia. The flow Reynolds number is 45.

as follows. The origin of the problem in the cylindrical formulation is the directional dependence of the relative particle velocity on the orientation of the separation vector. For fluid elements, this anisotropy of relative velocity statistics is due to the difference in the radial (or longitudinal) strain rate and the transverse strain rate (Wang *et al.* 1998*b*). Finite-inertia particles, however, do not respond only to the local fluid flow. They respond to a wider range of eddy motion along their previous trajectories. Furthermore, the orientation of the particle separation vector is random before the two particles come into contact. This combination seems to remove very quickly the orientational dependence of the Lagrangian particle-pair relative velocity. For $\tau_p/\tau_k > 1$, the two formulations are almost identical. As a side note, we recall that the statistics of relative velocity components between fluid elements always depend on the orientation of the separation, no matter whether the separation is in the order of the Kolmogorov length or the integral length (Hinze 1975).

Figure 4 shows the ratios for a much larger particle inertia range. Both formulations appear to predict exactly the collision kernel for $\tau_p/\tau_k > 1$, given the statistical uncertainties in the simulations.

A minor, but definite feature in figure 3 is that there is a dip around $\tau_p/\tau_k \approx 0.5$ for both curves. For the spherical formulation, this dip causes a slight underprediction of the collision kernel. The maximum deviation from one is about 4% at $\tau_p/\tau_k = 0.6$. Since the standard deviation is only 1% at $\tau_p/\tau_k = 0.6$, the deviation is significant and due to the fact that the particle concentration has not reached the asymptotic stationary stage, as indicated in § 2.

To confirm this, we plot the ratios of w_r^-/w_r^+ and $C_p = Pw_r^-/[(1-P)w_r^+]$ in figure 5. Note that we used a much larger number of particles in the simulations for $\tau_p/\tau_k < 1.3$ than for $\tau_p/\tau_k > 1.3$, thus the statistical uncertainties are much smaller for

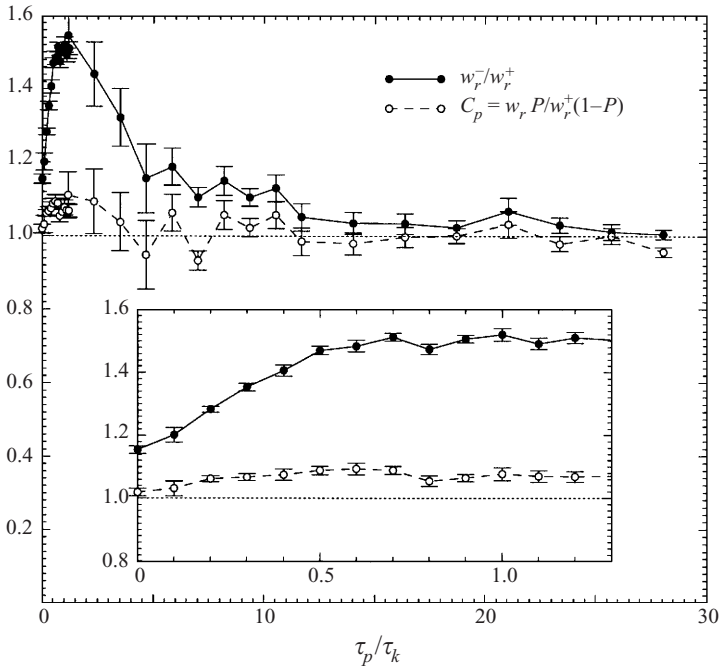

FIGURE 5. The two ratios, w_r^-/w_r^+ and $C_p = Pw_r - /[(1-P)w_r^+]$, as a function of τ_p/τ_k. The flow Reynolds number is 45.

$\tau_p/\tau_k < 1.3$. It is very clear that $w_r^-/w_r^+ > 1$ when $\tau_p/\tau_k = O(1)$, as a result of local accumulation in the region of low flow vorticity and high strain rate (Maxey 1987; Wang & Maxey 1993). At least for very weak inertia ($\tau_p/\tau_k \ll 1$), the particle velocity divergence field can be defined and related to the fluid strain rate and vorticity field as (Maxey 1987)

$$\nabla \cdot \boldsymbol{v} = \tau_p(\tfrac{1}{2}\omega^2 - s_{ij}s_{ij}), \tag{4.1}$$

where $\boldsymbol{\omega} = \nabla \times \boldsymbol{u}$ and $s_{ij} = (\partial u_i/\partial x_j + \partial u_j/\partial x_i)/2$ are the local fluid vorticity and rate of strain field, respectively. This indicates that the local velocity divergence seen by particle pairs at contact tends to be negative. As a result, w_r^- would be larger than w_r^+. This bias is physically expected.

On the other hand, the ratio of relative fluxes, C_p, should be equal to one if the concentration field is statistically stationary. Figure 5, however, shows a slightly larger inward flux owing to the transition to the stationary stage. This effect can be corrected in the spherical formulation by (2.8). The corrected results are compared with the DNS collision kernel in figure 6. Clearly, the dip has been removed. This correction could also be applied to the cylindrical formulation.

We found very similar results for other flow Reynolds numbers. For fluid elements ($\tau_p/\tau_k = 0$), the cylindrical formulation overpredicts the collision kernel by 25%, 22%, 23%, and 21% for $R_\lambda = 24$, 45, 58, and 75, respectively. The level of overprediction is given by $\langle|\boldsymbol{w}|\rangle/(2\langle|w_r|\rangle) - 1$. A simple model based on Gaussian probability density function (p.d.f.) of relative velocity then predicts 28.6% overprediction (Wang *et al.* 1998*b*). For very small fluid elements, the p.d.f. of w_r is the same as the p.d.f. of the radial (or longitudinal) fluid velocity gradient (e.g. $\partial u/\partial x$). Figure 7(*a*) shows the p.d.f.s of the radial velocity gradient for the DNS flow fields. The velocity gradients

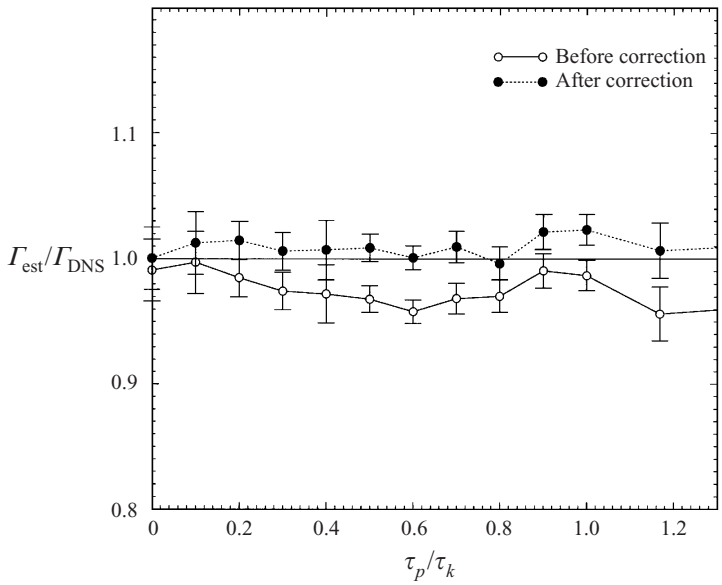

FIGURE 6. Comparison of the spherical formulation with DNS results before and after the flux correction. The flow Reynolds number is 45.

were computed from Eulerian statistics and normalized by their respective r.m.s. value. The radial velocity gradient is negatively skewed, with a skewness of about −0.5 (Wang *et al.* 1996). The symmetry of the transverse velocity gradient is only a consequence of the flow isotropy. In agreement with previous experimental (Anselmet *et al.* 1984) and numerical results (Vincent & Meneguzzi 1991), the p.d.f. exhibits exponential tails, which becomes more evident as R_λ increases. A generic exponential p.d.f. was used by Sundaram & Collins (1997) as a model for the p.d.f. of relative velocity $\boldsymbol{w}$ at small τ_p/τ_k. In one dimension, the generic exponential p.d.f. can be written as

$$f(x) = \frac{n}{2}\frac{1}{p^3}\frac{1}{\Gamma(3/n)}\exp\left[-\left(\frac{|x|}{p}\right)^n\right], \quad \text{with} \quad p \equiv \sqrt{\frac{\Gamma(1/n)}{\Gamma(3/n)}}, \tag{4.2}$$

where Γ is the gamma function. Note that both the coefficient of $f(x)$ and the definition of p differ from those given in Sundaram & Collins (1997) for a three-dimensional vector field $\boldsymbol{x}$. This p.d.f. has a unit standard deviation and $\int_{-\infty}^{\infty} f(x)\,\mathrm{d}x = 1$. When $n = 1$, the p.d.f. is a simple exponential, whereas $n = 2$ represents a standard Gaussian p.d.f. For $|w_r| < 2\langle w_r^2\rangle^{1/2}$, the Gaussian curve appears to match the data better than the simple exponential p.d.f. ($n = 1$). We note that the Gaussian p.d.f. model predicts $\langle|w_r|\rangle/\langle w_r^2\rangle^{1/2} = 0.798$ and the exponential p.d.f. model predicts $\langle|w_r|\rangle/\langle w_r^2\rangle^{1/2} = 0.707$ (L. R. Collins 1998, personal communications). The actual value of $\langle|w_r|\rangle/\langle w_r^2\rangle^{1/2}$ for the DNS flow fields is about 0.77 (Wang *et al.* 1998*b*), which is better predicted by the Gaussian p.d.f. model. This is due to the facts that (i) the ratio is determined mainly by the p.d.f. at small to intermediate w_r; and (ii) the asymmetry causes the Gaussian model to be better for large positive w_r, although the exponential p.d.f. is a better model for large negative w_r.

To be complete, we also show the p.d.f. of the transverse velocity gradient (e.g. $\partial u/\partial y$) in figure 7(*b*). The p.d.f. is now symmetric. The exponential model appears

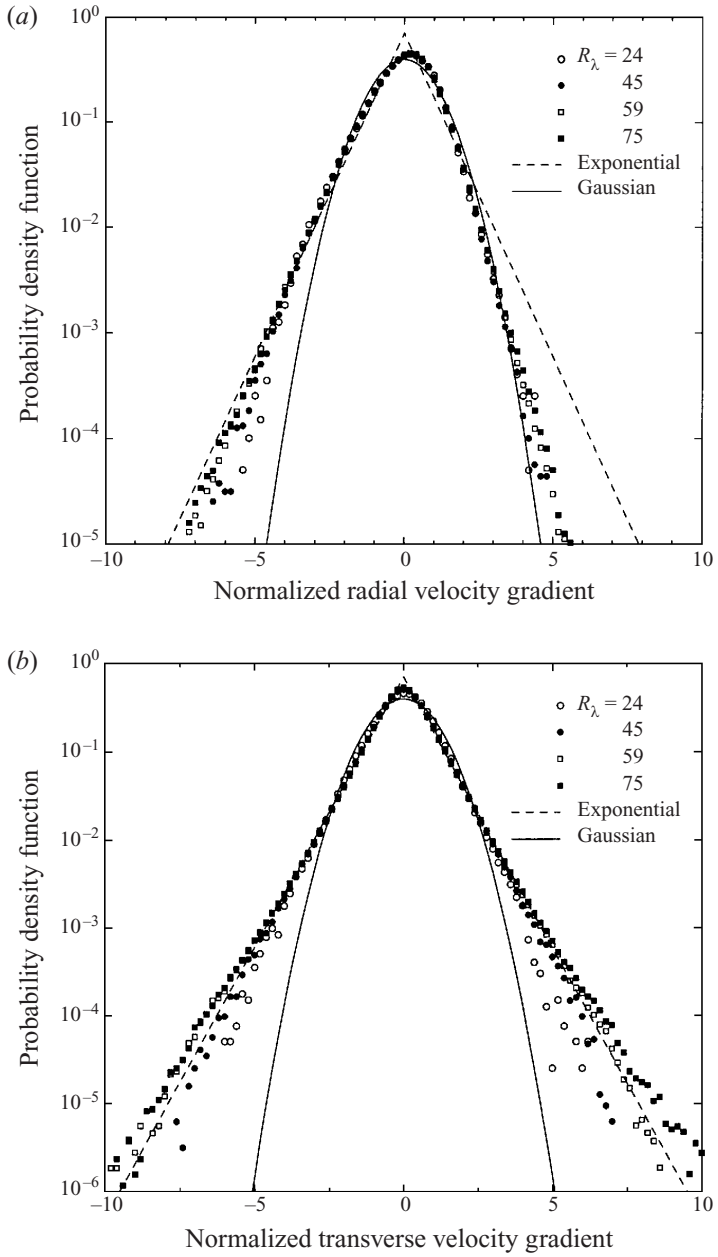

FIGURE 7. The probability distribution functions (p.d.f.s) for different flow Reynolds numbers: (*a*) the radial velocity gradient; (*b*) the transverse velocity gradient.

to be a better model than the Gaussian model, especially for large magnitudes of relative velocity. This is consistent with the observation of Sundaram & Collins (1997). This implies that the exponential model might give a better prediction for $\langle|\boldsymbol{w}|\rangle/(2\langle|w_r|\rangle) - 1$, although we are unable to evaluate this analytically.

For finite-inertia particles, we observed similar results regarding the comparison of the two formulations and the flux correction. We found that the flux correction

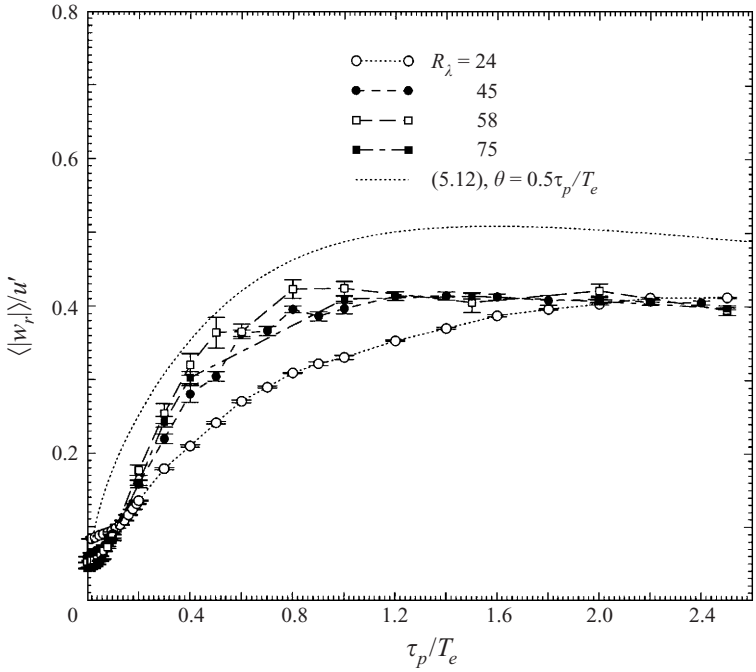

FIGURE 8. The normalized radial relative velocity, $\langle|w_r|\rangle/u'$ as a function of particle inertia.

was the largest for lowest flow Reynolds number ($R_\lambda = 24$) owing to very limited separation in scales and thus the large-scale fluid motion presented the strongest influence on the transition of the concentration field from uniform to the asymptotic non-uniform stage. At larger flow Reynolds numbers, the flux balance appeared to be established sooner.

4.2. *The turbulent transport effect*

Now we study separately the turbulent transport effect and the accumulation effect. The turbulent transport effect is quantified by the radial relative velocity $\langle|w_r|\rangle$. Figure 8 shows the radial relative velocity, normalized by the fluid r.m.s. velocity, as a function of the particle inertial response time (τ_p/T_e) for different flow Reynolds numbers. The relative velocity increases quickly with particle inertia for $\tau_p < T_e$ because large-scale turbulent fluctuations contribute to the particle motion. In addition the velocities of the two particles become less correlated as τ_p increases (figure 9), which also contributes to the increase [see (2.9)]. For $\tau_p > T_e$, the relative velocity starts to decrease slowly with τ_p as there are no more large-scale fluctuations in the flow and particle response to the flow becomes sluggish. Except for the case of $R_\lambda = 24$, the dimensionless particle radial relative velocity is almost independent of R_λ for $\tau_p = O(T_e)$, confirming the large-scale scaling of $\langle|w_r|\rangle$. Our simple eddy–particle interaction model predicts the shape reasonably well.

Figure 9 shows the correlation coefficient ρ_{12} of particle radial relative velocities (see equation (2.11)) as a function of τ_p for different Reynolds numbers. Again, the $R_\lambda = 24$ flow field shows different behaviour from the others, while for the three other higher flow Reynolds numbers, the data for ρ_{12} collapse well. For zero inertia, the

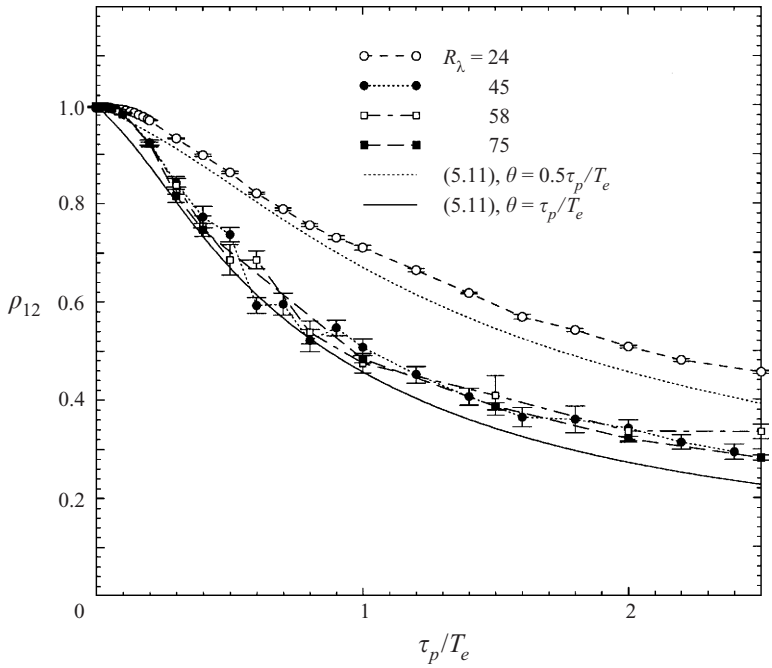

FIGURE 9. The correlation coefficient, ρ_{12}, as a function of particle inertial.

correlation coefficient can be shown, using Taylor expansion, to be

$$\begin{aligned}\rho_{12} &\approx 1 + \frac{R^2}{2u'^2}\left\langle u\frac{\partial^2 u}{\partial x^2}\right\rangle \\ &= 1 - \frac{R^2}{2u'^2}\left\langle \frac{\partial u}{\partial x}\frac{\partial u}{\partial x}\right\rangle \\ &= 1 - \left(\frac{R}{\eta}\right)^2 \frac{1}{2\sqrt{15}R_\lambda},\end{aligned} \tag{4.3}$$

which is 0.9947, 0.9971, 0.9978, and 0.9983 for $R_\lambda = 24, 45, 58$, and 75, respectively. The corresponding simulation results based on Lagrangian particle pairs are 0.9949 ± 0.0001, 0.9970 ± 0.0001, 0.9978 ± 0.00005, and 0.9983 ± 0.00005. The qualitative agreement (up to 4 significant digits) between the numerical predictions and the trend of the theory validates the simulation code, while their quantitative agreement shows the level of numerical accuracy. As τ_p increases, particles start to respond to random eddies before coming into contact and thus the velocities at contact are less correlated. At large inertia, the correlation coefficient decays rather slowly, partly due to the use of frozen flow fields. This slow decorrelation makes the prediction of relative velocity based on kinetic theory (Abrahamson 1975) only applicable for extremely large τ_p/T_e. Our simple eddy–particle interaction model gives reasonable prediction of ρ_{12}. Since the model was developed based on a one-dimensional eddy–particle interaction, the definition of θ may be adjusted to fit the data better. Indeed, a slight modification of θ from $\theta = 0.5\tau_p/T_e$ to $\theta = \tau_p/T_e$ improves the prediction. We, therefore, expect that the slow decorrelation may be observed even for evolving flow fields.

In figure 10 we compare the simulation results of total relative velocity with analytical predictions of Williams & Crane (1983) and Kruis & Kusters (1997). Note

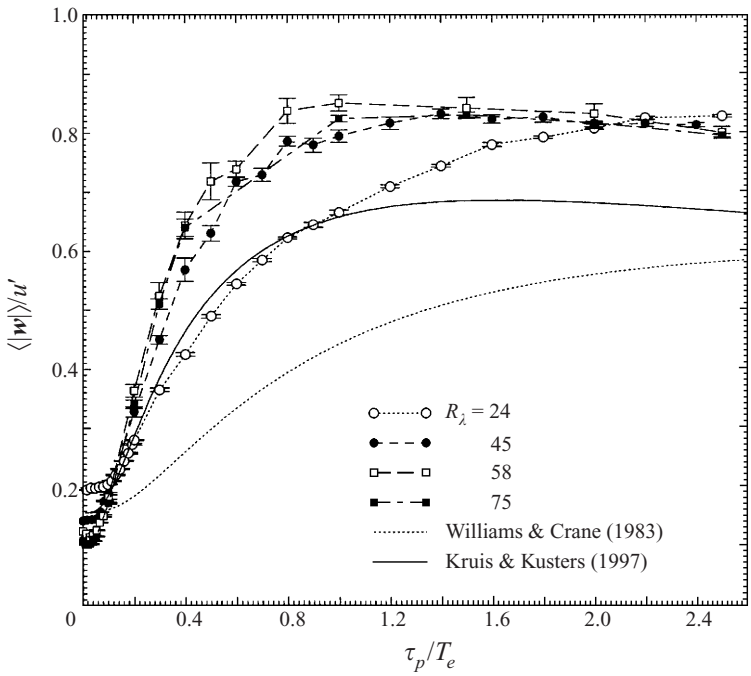

FIGURE 10. The normalized total relative velocity, $\langle|\boldsymbol{w}|\rangle/u'$, as a function of particle inertia.

that both Williams & Crane (1983) and Kruis & Kusters (1997) related the collision kernel to the total relative velocity $\langle|\boldsymbol{w}|\rangle$ using the cylindrical formulation. Although Kruis & Kusters' prediction agrees well with DNS results for $\tau_p/\tau_k < 1$ at $R_\lambda = 24$, it underpredicts the relative velocity for higher Reynolds numbers and large particle inertias by about 18%. The prediction of Williams & Crane (1983) is worse when compared with our data.

We shall now discuss how the p.d.f.s of relative velocities change with the particle inertia parameter and flow Reynolds numbers. Figure 11 shows the p.d.f.s of both the transverse relative velocity w_t and the radial relative velocity w_r at $\tau_p = 0.1\tau_k$. The transverse relative velocity w_t is defined as $|\boldsymbol{w} \times \boldsymbol{R}|/|\boldsymbol{R}|$. Since the particle inertia is weak, particles almost follow the local fluid velocity. Therefore, the p.d.f.s are quite similar to those in figure 7 for fluid elements. Since the p.d.f.s for fluid elements were computed based on Eulerian field data, a good comparison at weak inertia also validates our numerical code for computing p.d.f.s of Lagrangian particle-pair relative velocity.

Figure 12 shows the p.d.f.s at $\tau_p = \tau_k$. The most interesting feature is that now the tails of p.d.f.s are much more stretched. In fact, a fit of the generic exponential form (4.2) to the transverse p.d.f.s yields a value of $n = 0.40 - 0.70$ (table 3). A smaller n indicates that the relative velocity is more intermittent, namely, with large probabilities of observing small and very large values. This is a result of local accumulation, which drives particles to regions around intense vortex tubes and other high-strain-rate regions (Squires & Eaton 1991; Wang & Maxey 1993). Another observation is that the p.d.f.s for R_λ =45, 58, and 75 overlap very well with each other, even in the tails. This overlap is also better than in the case of fluid elements. This demonstrates an R_λ independence, or certain features of small-scale structures have already reached their asymptotic characteristics even at moderate flow Reynolds

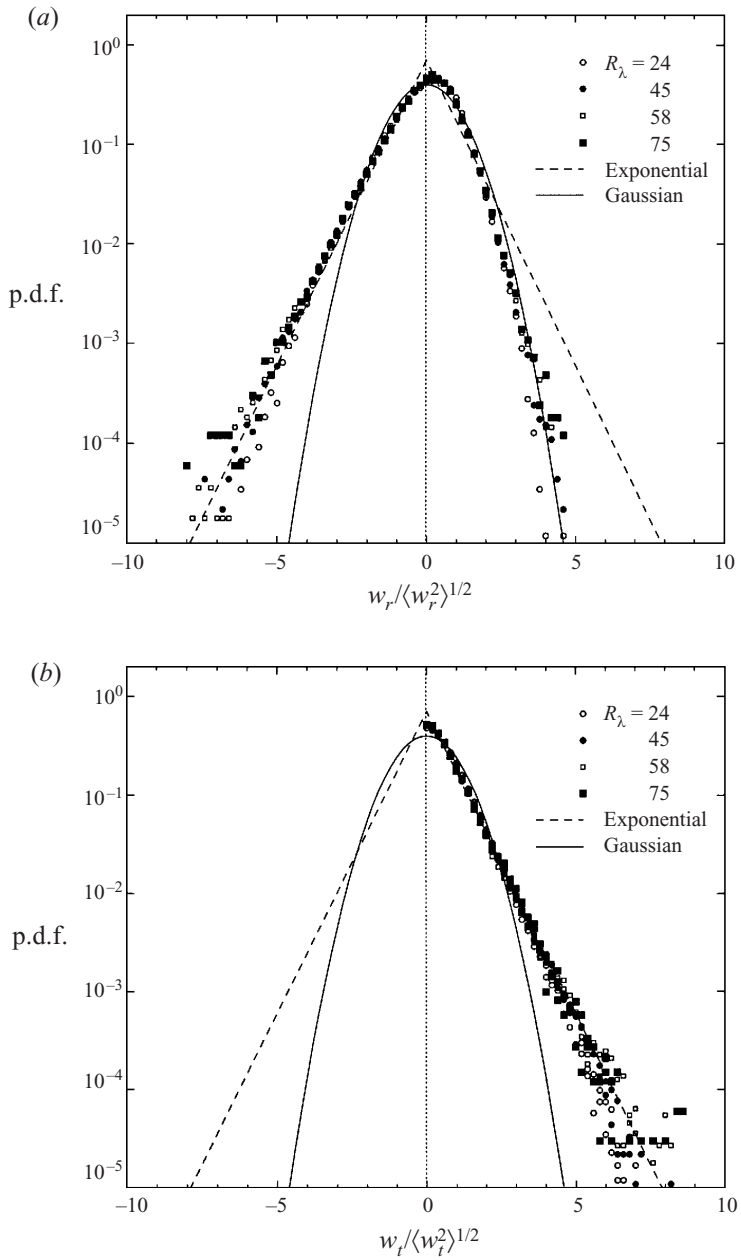

FIGURE 11. The p.d.f.s of relative velocity at $\tau_p/\tau_k = 0.1$ ($\tau_p/T_e = 0.016$ at $R_\lambda = 24$, $\tau_p/T_e = 0.0086$ at $R_\lambda = 45$, $\tau_p/T_e = 0.0066$ at $R_\lambda = 58$, $\tau_p/T_e = 0.0051$ at $R_\lambda = 75$): (*a*) the radial relative velocity; (*b*) the transverse relative velocity. The relative velocities are normalized by their respective standard deviation.

numbers. This observation is important and shows the value of conducting careful DNS even at low flow Reynolds numbers. A similar point was noted in the work of Wang *et al.* (1996) who studied more completely the relative velocity statistics of fluid elements in DNS. The asymmetry in the p.d.f.s of radial relative velocity is noticeable at this particle inertia, as shown by the large negative skewness in table 4.

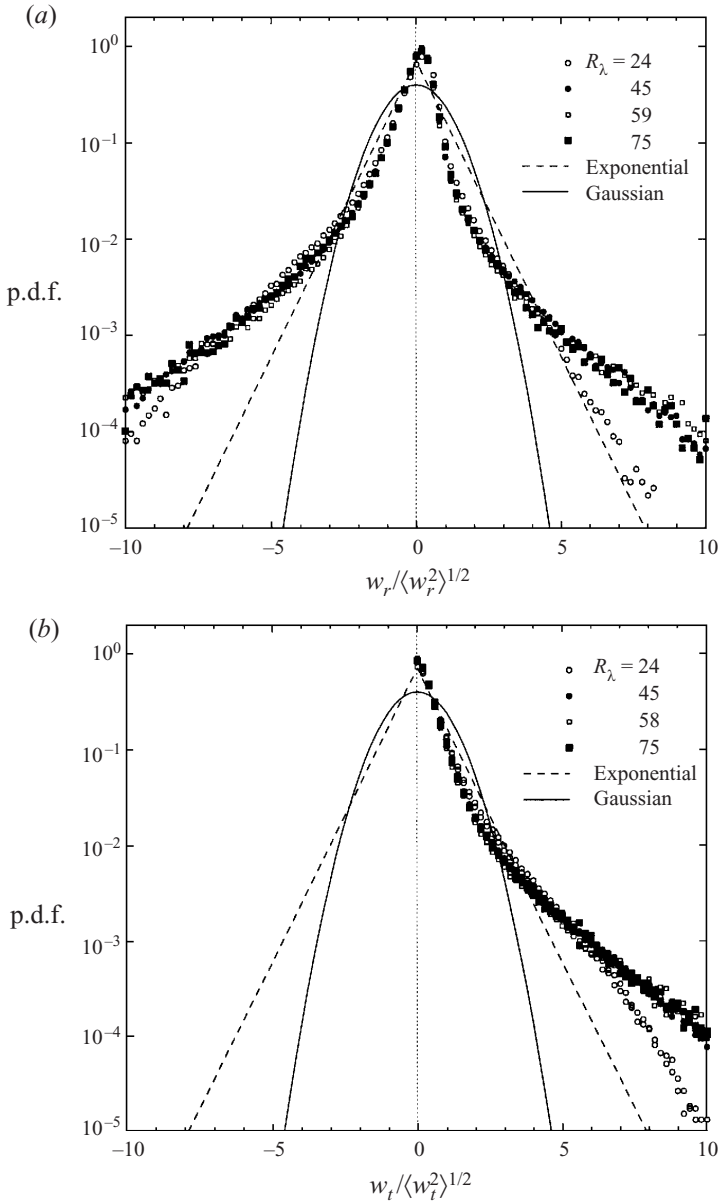

FIGURE 12. The p.d.f.s of relative velocity at $\tau_p/\tau_k = 1.0$ ($\tau_p/T_e = 0.16$ at $R_\lambda = 24$, $\tau_p/T_e = 0.086$ at $R_\lambda = 45$, $\tau_p/T_e = 0.066$ at $R_\lambda = 58$, $\tau_p/T_e = 0.051$ at $R_\lambda = 75$): (*a*) the radial relative velocity; (*b*) the transverse relative velocity.

R_λ	Fluid elements	$\frac{\tau_p}{\tau_k} = 0.1$	$\frac{\tau_p}{\tau_k} = 1.0$	$\frac{\tau_p}{T_e} = 1.0$	$\frac{T_p}{T_e} = 2.5$
24	1.0	1.2	0.7	1.1	1.5
45	1.0	1.0	0.43	1.35	1.8
58	1.0	1.0	0.37	1.45	1.8
75	1.0	1.0	0.40	1.45	1.8

TABLE 3. The exponential index n for different Reynolds numbers and particle inertias.

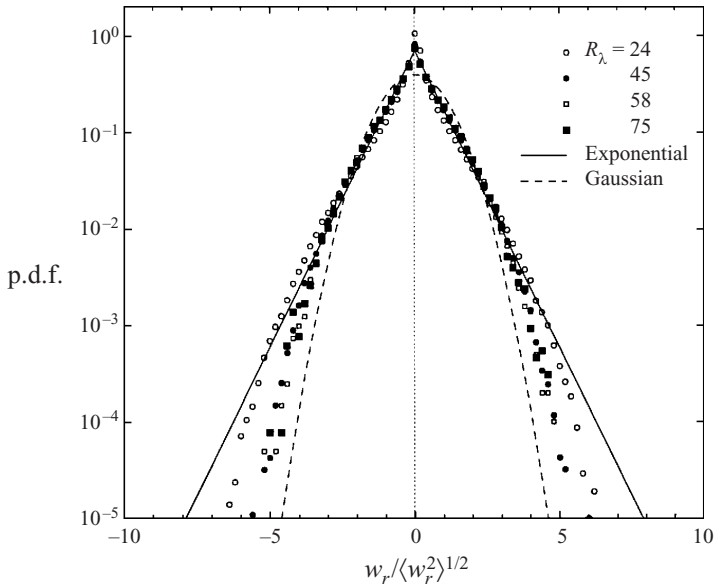

FIGURE 13. The p.d.f.s of radial relative velocity at $\tau_p/T_e = 1$ ($\tau_p/\tau_k = 6.3$ at $R_\lambda = 24$, $\tau_p/\tau_k = 11.6$ at $R_\lambda = 45$, $\tau_p/\tau_k = 15.1$ at $R_\lambda = 58$, $\tau_p/\tau_k = 19.5$ at $R_\lambda = 75$).

R_λ	Fluid elements	$\frac{\tau_p}{\tau_k} = 0.1$	$\frac{\tau_p}{\tau_k} = 1.0$	$\frac{\tau_p}{T_e} = 1.0$	$\frac{T_p}{T_e} = 2.5$
24	−0.47	−0.66	−1.86	−0.16	−0.05
45	−0.48	−0.71	−1.86	−0.06	−0.02
58	−0.53	−0.72	−1.27	−0.05	−0.08
75	−0.48	−0.58	−2.03	−0.02	−0.03

TABLE 4. The skewness of radial relative velocity fluctuations.

The p.d.f.s for much larger particle inertia, $\tau_p = T_e$, are shown in figure 13. The important observation is that the asymmetry in the radial relative velocity p.d.f. disappears and the p.d.f.s for the radial relative velocity and the transverse relative velocity (not shown) are almost identical. This is consistent with the observation that the cylindrical and spherical formulations are identical at large particle inertia. Unexpectedly, the p.d.f.s are closer to the simple exponential curve than the Gaussian curve, particularly for relative velocities within three standard deviations. For very large relative velocity, the p.d.f.s appear to approach the Gaussian curve as R_λ increases.

The p.d.f.s for even larger particle inertia, $\tau_p = 2.5T_e$, are shown in figure 14. Very interestingly, the tails now match the Gaussian curve, particularly for larger R_λ cases, in agreement with the observation of Sundaram & Collins (1997). However, for relative velocities within two standard deviations, the p.d.f.s fit better to the exponential curve. This could be due to the influence of persistent large-scale eddies in the frozen flow fields, i.e. some particles may be trapped by them and their relative motion is strongly correlated, as shown by the ρ_{12} plot. The asymmetry completely disappears for the radial relative velocity. Putting all the plots together, we conclude that as τ_p/T_e increases further, the p.d.f. will eventually be Gaussian.

In summary, there is a strong dependence of the shape of the p.d.f. on the particle

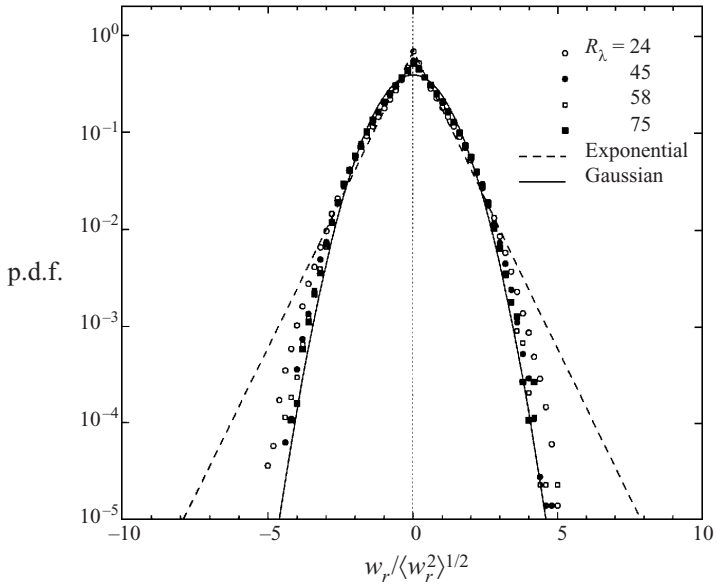

FIGURE 14. The p.d.f.s of radial relative velocity at $\tau_p/T_e = 2.5$ ($\tau_p/\tau_k = 15.6$ at $R_\lambda = 24$, $\tau_p/\tau_k = 29.0$ at $R_\lambda = 45$, $\tau_p/\tau_k = 37.8$ at $R_\lambda = 58$, $\tau_p/\tau_k = 48.8$ at $R_\lambda = 75$).

inertia. If measured by the exponent n of the generic exponential curve (4.2), n decreases with inertia for weak inertia, reaches a minimum at $\tau_p/\tau_k = O(1)$, then increases with τ_p for $\tau_p > \tau_k$. This dependence was first noted by Sundaram & Collins (1997), although no quantitative information on n for finite inertia was provided in their paper. In table 3 we provide quantitative estimates of n. The values were obtained by trial and error to best match the simulated p.d.f.s with the generic exponential, (4.2), for relative velocities larger than two standard deviations. The exponent also depends on Reynolds number, namely, as R_λ increases, the exponent is smaller at $\tau_p = \tau_k$ but returns to the Gaussian value ($n = 2$) more quickly at large inertia. At small particle inertia, the p.d.f. for the radial relative velocity differs from that for the transverse relative velocity in two ways: first the variance is different, secondly the p.d.f. is asymmetric for the radial component but is symmetric for the transverse component. Figure 15 shows the ratio of the variances, $\langle w_t^2\rangle/\langle w_r^2\rangle$, as a function of τ_p/τ_k. For fluid elements, this ratio is two (Hinze 1975). The ratio drops very quickly towards one as τ_p approaches τ_k, consistent with the comparison of the two formulations shown in figure 3. This ratio is R_λ-independent except for the scatters due to statistical uncertainties. The skewness of the relative velocities are listed in table 4. In agreement with previous experimental (Anselmet *et al.* 1984) and numerical (Wang *et al.* 1996) results, the skewness is about -0.5 for fluid elements. Its magnitude increases with particle inertia and reaches a maximum at $\tau_p = \tau_k$, then drops back to zero at large inertia. The skewness itself, however, has no direct effect on the formulation of the collision kernel.

4.3. *The accumulation effect*

Figure 16 shows the radial distribution function at contact, $g(R)$, as a function of particle inertial response time (τ_p/τ_k) for four different flow Reynolds numbers. All the curves have a very similar shape. For very weak inertia ($\tau_p/\tau_k \ll 1$), the particle concentration field is statistically uniform, so $g(R) = 1$. As τ_p increases, $g(R)$ increases

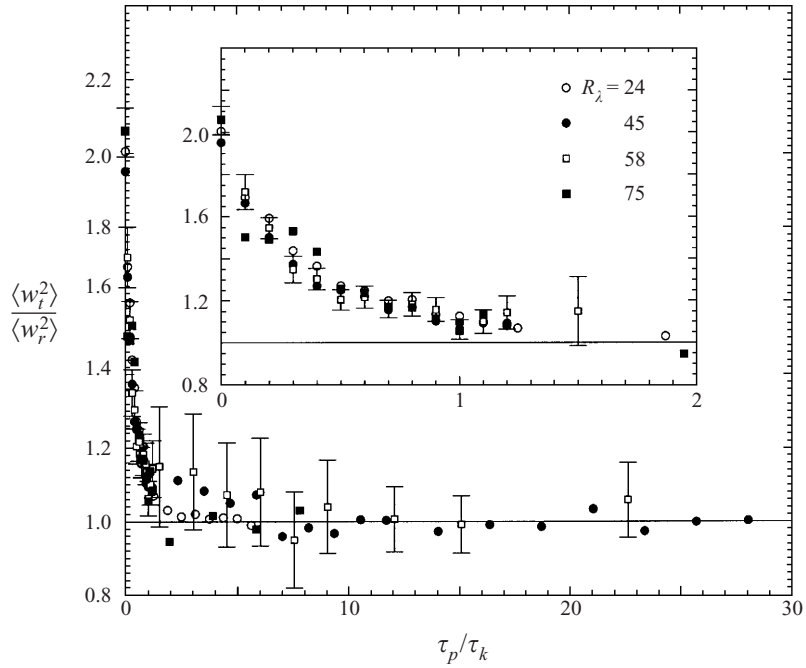

FIGURE 15. The variance ratio as a function of particle Stokes number.

very quickly. A maximum is reached at $\tau_p/\tau_k \approx 1$. For $\tau_p/\tau_k > 1$, $g(R)$ decreases with particle inertia. This behaviour is quite similar to the dependence of global accumulation measures on particle inertia, as shown in Wang & Maxey (1993). This is expected since $g(R)$ is a measure of the preferential concentration on pair density distribution and can be viewed as a global measure of the accumulation. Since the preferential concentration is a result of dissipation-range flow structures, the peak location is scaled by the flow Kolmogorov scale. Wang & Maxey (1993) reported that the peak value in global accumulation occurs at $\tau_p/\tau_k \approx 0.8$, slightly less than $\tau_p/\tau_k \approx 1$ here. This could be due to the fact that frozen flow fields were used in this work but evolving flow fields were used in Wang & Maxey (1993).

Our results also agree well with the $g(R)$ curve for evolving flow reported by Sundaram & Collins (1997) . With very few data points around $\tau_p/\tau_k = 1$, they found that the maximum $g(R)$ occurred at $\tau_p/\tau_k = 0.4$. Since an extrapolation was used in their work for $g(R)$ computation and a significant uncertainty was noted, their peak location should not be compared with ours quantitatively. In addition, their $g(R)$ at $\tau_p/\tau_k = 0.4$ was overestimated owing to the artificial repeated collisions under the hard-sphere model used in their work (see Sundaram & Collins 1997 and Zhou *et al.* 1998 for further discussions). A comparison of the DNS collision kernels between our collision-detection scheme and the hard-sphere model at $R_\lambda = 45$ showed that at $\tau_p/\tau_k = 0.4$ the artificial repeated collisions almost double the collision rate (see figure 4 in Zhou *et al.* 1998). We can compare directly the results at $\tau_p/\tau_k = 1$ as the artificial effect due to the hard-sphere model is no longer important (Zhou *et al.* 1998). At $\tau_p/\tau_k = 1$, our $g(R)$ is 9.3 at $R_\lambda = 58$ and Sundaram & Collins (1997) had $g(R) \approx 7.6$ at $R_\lambda = 54$. This level of difference is consistent with the difference in collision kernels between the frozen flow and the evolving flow at $\tau_p/\tau_k = 1$, as shown in Zhou *et al.* (1998). In general, we expected that, relative to frozen flow fields, the

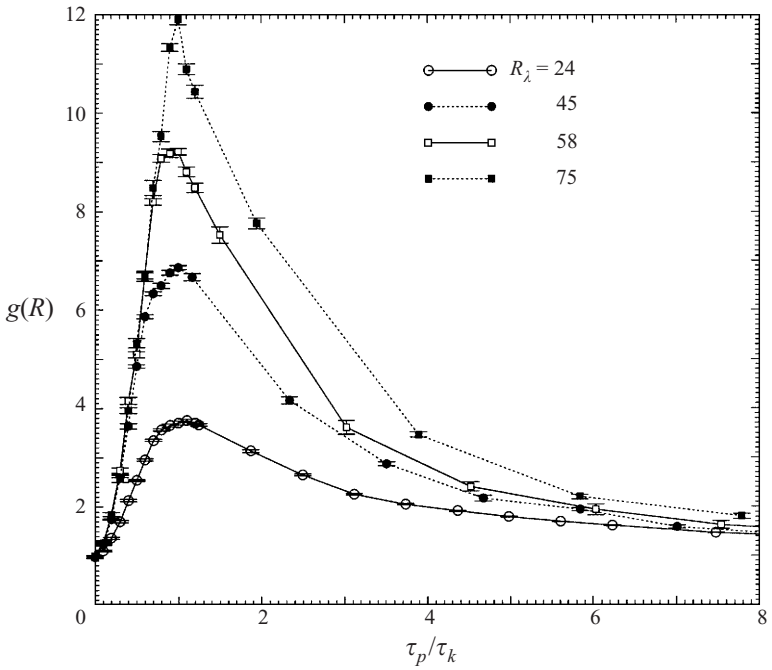

FIGURE 16. The radial distribution function at contact, $g(R)$, as a function of particle inertia.

peak value of $g(R)$ is smaller in evolving flow since small-scale vortex tubes have finite lifetime and the accumulation is a dynamic process.

In agreement with the results of Wang & Maxey (1993), the peak value increases with Reynolds number. A more careful examination of the R_λ dependence will be presented in the next section.

Another interesting observation is that the uncertainties here are much smaller than those in the relative velocity statistics. This can be explained as follows. In a given flow, the number of small-scale dissipation range eddies is much larger than the number of large-scale eddies. Since $g(R)$ is determined by interactions of particles with small-scale eddies, while the relative velocity statistics are governed by interactions with large-scale eddies, there are many more statistically independent samples for $g(R)$ computation than that for relative velocity statistics.

5. Model development

In this section, we will develop empirical models for both $g(R)$ and $\langle |w_r| \rangle$ in order to predict the collision kernel accurately. The model will then be compared with the DNS collision kernel and also used to speculate results at much higher flow Reynolds numbers than is possible in our numerical simulations.

5.1. *Asymptotic behaviour of* $g(R)$ *for small particle inertia*

First, we present an asymptotic result for $g(R)$ at $\phi \equiv \tau_p/\tau_k \ll 1$. Recall that $g(R)$ is the probability of observing particle pairs with separation near R, normalized by the reference probability in a random uniform suspension. Since R is small, the local

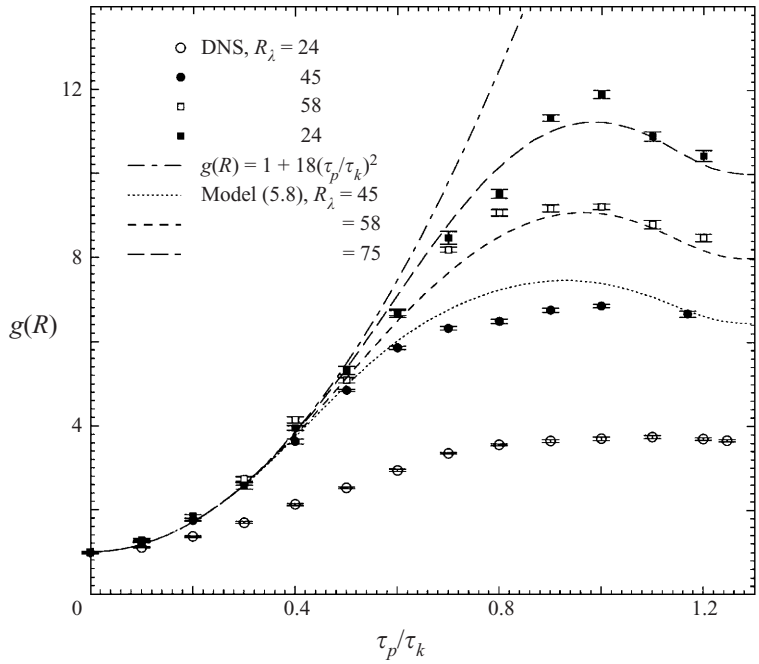

FIGURE 17. The radial distribution function at contact, $g(R)$, as a function of particle inertia for $\tau_p/\tau_k < 1.3$.

probability is proportional to $[n(\boldsymbol{x}, t)]^2$. We can make the following approximation,

$$g(R) \approx \frac{\langle n^2 \rangle}{n_0^2}, \tag{5.1}$$

where $n(\boldsymbol{x}, t)$ is the local particle number concentration. For $\phi \ll 1$, the local concentration can be related to local flow vorticity and rate of strain

$$n \approx n_0[1 + \tau_p \tau_f (s_{ij}s_{ij} - \tfrac{1}{2}\omega^2)], \tag{5.2}$$

where τ_f is a history timescale of the order τ_k (Zhou *et al.* 1998). Substituting (5.2) into (5.1), we obtain a leading-order approximation for $g(R)$ at $\phi \ll 1$:

$$\begin{aligned} g(R) &\approx \langle [1 + C_1 \tau_p \tau_k (s_{ij}s_{ij} - \tfrac{1}{2}\omega^2)]^2 \rangle \\ &\approx 1 + C_2 \cdot \phi^2, \end{aligned} \tag{5.3}$$

where C_1 and C_2 are dimensionless constants. In deriving (5.3), we made use of the facts that $(s_{ij}s_{ij} - \omega^2/2)$ is scaled with τ_k^{-2} and $\langle s_{ij}s_{ij} - \omega^2/2 \rangle = 0$. Hence, we expect that $g(R)$ increases with ϕ quadratically at small particle inertia. In addition, under that limit, C_2 is independent of R_λ.

The numerical simulation results are compared with this asymptotic theory in figure 17. $C_2 = 18$ is obtained by fitting (5.3) to the DNS results for small ϕ. In agreement with the previous observation, when a similar asymptotic theory was applied to the collision kernel (Zhou *et al.* 1998), $g(R)$ is independent of R_λ for $R_\lambda \geqslant 45$ and $\phi \leqslant 0.5$. The quadratic behaviour is clearly seen. At very low Reynolds number, there is not enough scale separation in the flow for the above asymptotic expansion to apply.

5.2. *An empirical model for* $g(R)$

An important observation from figure 17 is that, except for a small region of $\phi < 0.5$ as discussed above, $g(R)$ depends on flow Reynolds number. A careful examination reveals a surprisingly simple scaling, namely, $g(R) - 1$ scales linearly with R_λ, as shown in figure 18. The data for the three higher flow Reynolds numbers collapse extremely well, while the data for the lowest flow Reynolds number do not show such a good collapse and are not included in this figure, owing to very limited separation of flow scales. We cannot conclude definitely that this scaling is valid for all high flow Reynolds numbers, since our simulations cover a small range of flow Reynolds numbers. Nevertheless, this simple scaling appears to separate out the R_λ dependence.

Therefore, we may propose the following simple relationship for $\phi > 0.5$:

$$\frac{g(R)-1}{R_\lambda} = F(\phi). \tag{5.4}$$

For the purpose of having a closed-form empirical model, we express $F(\phi)$ explicitly. This was constructed as follows. First, for $0.5 < \phi < 1.25$, an analytical form is assumed:

$$y_1(\phi) = 0.36\phi^{2.5}\exp(-\phi^{2.5}) \quad \text{for } 0.5 < \phi < 1.25. \tag{5.5}$$

This form has a maximum at $\phi = 1$. For $\phi > 1.25$, there appear to be two exponential decay regions, one for $1.25 < \phi < 5$ and the second for $\tau_p/\tau_k > 10$. These regions can be fitted by the following simple exponential functions (figure 18):

$$y_2(\phi) = 0.24\exp(-0.5\phi) \quad \text{for } 1.25 < \phi < 5, \tag{5.6}$$

$$y_3(\phi) = 0.013\exp(-0.07\phi) \quad \text{for } \phi > 10. \tag{5.7}$$

A composite fit is then constructed in the following manner:

$$\frac{g(R)-1}{R_\lambda} = \frac{y_0(\phi)[1-z_0^2(\phi)]}{R_\lambda} + z_0^2(\phi)\{y_1(\phi)[1-z_1(\phi)] + y_2(\phi)z_1(\phi) + y_3(\phi)z_2(\phi)\}, \tag{5.8}$$

where $y_0(\phi) = 18\phi^2$ according to the asymptotic analysis, and $z_i(\phi)$ are smooth transition functions defined as

$$z_0(\phi) = \frac{1}{2}\left[1 + \tanh\frac{\phi - 0.5}{0.25}\right],$$

$$z_1(\phi) = \frac{1}{2}\left[1 + \tanh\frac{\phi - 1.25}{0.1}\right],$$

$$z_2(\phi) = \frac{1}{2}\left[1 + \tanh\frac{\phi - 6.5}{2.5}\right].$$

The first term in (5.8) is added to recover the asymptotic result at $\phi < 0.5$. The composite fit, (5.8), compares very well with the simulation data, as shown in figures 17 and 18. Note that figure 18(*b*) covers a much wider range of particle inertia than figure 16.

Although we are unable to provide a good explanation for the exponential decay in $g(R)$ for large particle inertia, we shall mention that similar behaviour has been observed for other systems. For a stochastic system of hard spheres, the non-overlapping assumption leads to $g(r) > 1$ for $r \geqslant R$. It is known that the radial distribution function appears to decay exponentially at large separation distance for a system of hard

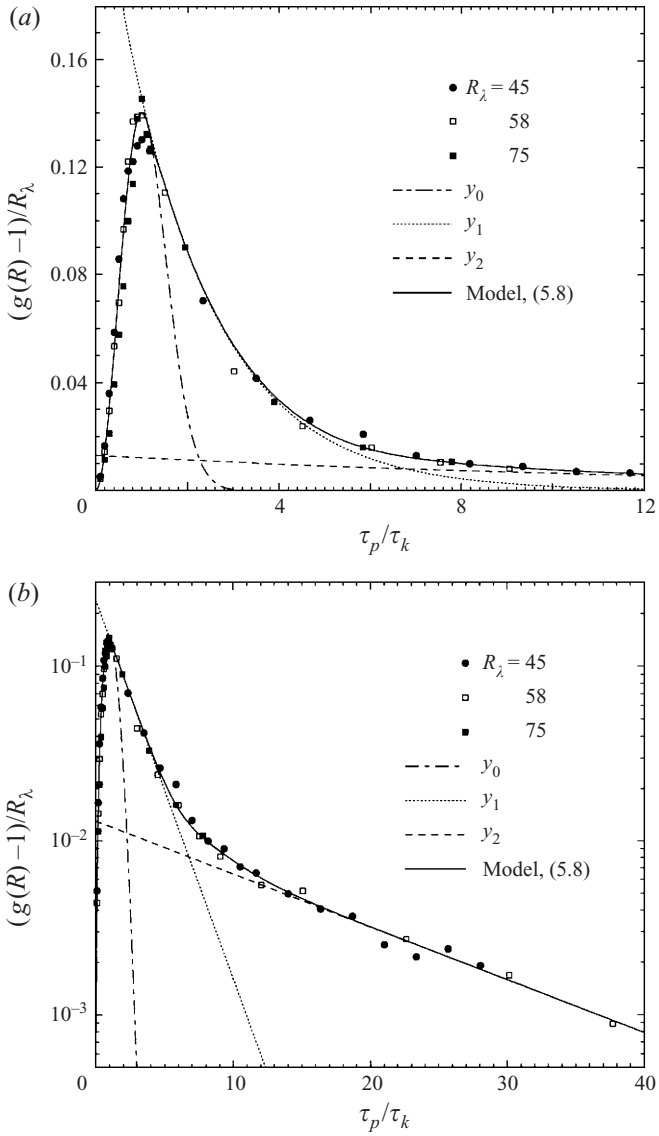

FIGURE 18. $[g(R)-1]/R_\lambda$ as a function of the particle inertia τ_p/τ_k. (*a*) linear–linear plot, (*b*) linear–log plot.

spheres (Tang & Lu 1995, 1997). In our large-inertia particle system, the motion of particles is determined mainly by large-scale, random events. The concentration distribution is nearly uniform and the small-scale vortical structures responsible for non-uniform concentration only introduce a weak perturbation to otherwise uniform concentration field. We speculate that a system of large-inertia particles bears some similarity to a system of hard spheres at large separation distance.

In the above empirical model, we chose $\phi = 0.5$ as the transition for the two scaling behaviours of $g(r)$. This transition was chosen based on simulation results at low Reynolds numbers and may not be the optimum value for high Reynolds number flows.

5.3. *Model for* $\langle |w_r| \rangle$

We have seen in figures 8 and 10 that no existing models can accurately predict the particle relative velocity, $\langle |w_r| \rangle$. However, one encouraging observation is that the shape of Kruis & Kusters prediction is very similar to that of the numerical results. Therefore, we modify Kruis & Kusters' theory to fit our simulation results. The result of Kruis & Kusters for the acceleration mechanism can be simplified in a monodisperse system without body force to

$$\frac{\langle w_{accel,i}^2 \rangle}{u'^2} = \frac{2\gamma\theta}{\gamma - 1}\left[1 - \frac{(1+2\theta)^{1/2}}{1+\theta}\right] \times \left[\frac{1}{(1+\theta)^2} - \frac{1}{(1+\gamma\theta)^2}\right], \tag{5.9}$$

where $\theta = 2.5\tau_p/T_e$ and $\gamma = 0.183u'^2/(\epsilon\nu)^{1/2} = 0.183u'^2/v_k^2$, the subscript i denotes individual components. Here, the acceleration mechanism refers to the effect of relative motion of particles from the local fluid motion, owing to finite particle inertia, on the particle pair relative velocity. The parameter γ signifies the R_λ dependence, since for fully developed turbulence we have (Hinze 1975, p. 225)

$$u'/v_k = R_\lambda^{0.5}/15^{0.25} \approx R_\lambda^{0.5}/2.0, \quad T_e/\tau_k = R_\lambda/15^{0.5} \approx R_\lambda/3.9. \tag{5.10}$$

We shall assume this same form applies to the radial relative velocity:

$$\frac{\langle w_{r,accel}^2 \rangle}{u'^2} = C_w \frac{2\gamma\theta}{\gamma - 1}\left[1 - \frac{(1+2\theta)^{1/2}}{1+\theta}\right] \times \left[\frac{1}{(1+\theta)^2} - \frac{1}{(1+\gamma\theta)^2}\right], \tag{5.11}$$

where a constant factor C_w is added to better fit the simulation data, the value of which is determined by curve fitting to simulation data. It is important to note that, for very large flow Reynolds number, $\gamma \gg 1$, equation (5.11) reduces to

$$\frac{\langle w_{r,accel}^2 \rangle}{u'^2} = C_w 2\theta\left[1 - \frac{(1+2\theta)^{1/2}}{1+\theta}\right] \times \frac{1}{(1+\theta)^2}. \tag{5.12}$$

This function increases with increasing particle inertia for $\theta < 3.61$, owing to the influence of increasing range of turbulent eddies on the particle motion, and then decreases with increasing particle inertia for $\theta > 3.61$, owing to an increasingly sluggish response of particles to turbulent fluctuations. There is a maximum of $0.128C_w$ at $\theta = 3.61$ or equivalently $\tau_p/T_e = 1.44$, thus the turbulent transport effect is most pronounced when $\tau_p/T_e = O(1)$.

For very small inertia particles, the relative velocity is related to the local shear rate in the flow. This shear contribution to the relative velocity is (Saffman & Turner 1956)

$$\frac{\langle w_{r,shear}^2 \rangle}{v_k^2} = \frac{1}{15}\left(\frac{R}{\eta}\right)^2. \tag{5.13}$$

It is significant that the shear contribution scales with the Kolmogorov velocity v_k while the acceleration mechanism scales with the large-scale fluctuation u'.

One way to include both the shear contribution and the acceleration mechanism is to specify the total relative velocity as

$$\langle w_r^2 \rangle = \langle w_{r,accel}^2 \rangle + \langle w_{r,shear}^2 \rangle. \tag{5.14}$$

This format was used by Saffman & Turner (1956) to combine several collision mechanisms. If we assume the p.d.f. of w_r is Gaussian, then we have

$$\langle |w_r| \rangle = \left(\frac{2}{\pi}\langle w_r^2 \rangle\right)^{1/2} = \left[\frac{2}{\pi}(\langle w_{r,accel}^2 \rangle + \langle w_{r,shear}^2 \rangle)\right]^{1/2}, \tag{5.15}$$

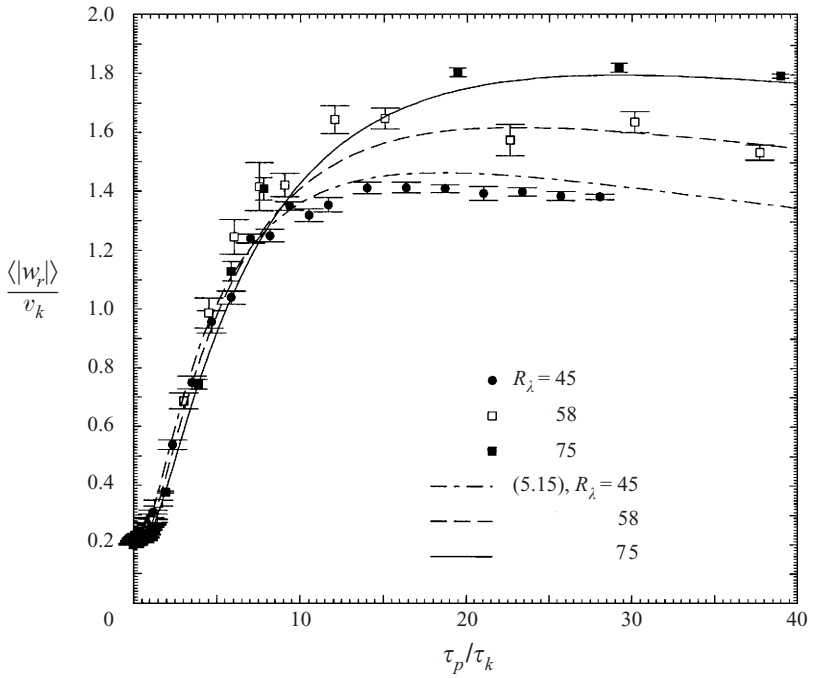

FIGURE 19. Comparison of the model prediction of $\langle|w_r|\rangle$ with the DNS data for different flow Reynolds numbers.

with $\langle w_{r,accel}^2\rangle$ and $\langle w_{r,shear}^2\rangle$ given by (5.11) and (5.13), respectively. By fitting the above relation to our simulation data at $R_\lambda = 58$, we obtain $C_w = 1.68$. In light of (5.10), we may express the above model in either of the following forms

$$\frac{\langle|w_r|\rangle}{u'} = F\left(\frac{\tau_p}{T_e}, R_\lambda, \frac{R}{\eta}\right), \quad \frac{\langle|w_r|\rangle}{v_k} = F\left(\frac{\tau_p}{\tau_k}, R_\lambda, \frac{R}{\eta}\right). \tag{5.16}$$

Obviously, the first form is more appropriate for large inertia ($\tau_p = O(T_e)$), whereas the second form is more appropriate for small inertia ($\tau_p = O(\tau_k)$). The dependence on R/η is known since this dependence appears only through the shear contribution.

In figure 19 we compare the above model with simulation results. The agreement is reasonable, given that many of the steps in Kruis & Kusters' derivation involves properties of turbulent flows at high Reynolds number. The model, however, is qualitatively correct at any R_λ.

5.4. *Collision kernel*

Since we have models for both the radial distribution function $g(R)$ and the radial relative velocity, we can now predict the collision kernel Γ using (2.5). The model predictions show satisfactory agreement with DNS collision kernels in figure 20.

5.5. *Qualitative prediction at high R_λ*

The model, while formulated and validated at relatively low Reynolds numbers ($R_\lambda < 75$), can now be used to describe qualitatively the collision kernels at high flow Reynolds numbers. We stress that the following predictions represent an extrapolation of our model. Figure 21 shows the model predictions of Γ, normalized by the collision kernel for fluid elements $\Gamma_0 = (8\pi/15)^{1/2}R^3 v_k/\eta$, as a function of τ_p/τ_k for R_λ ranging

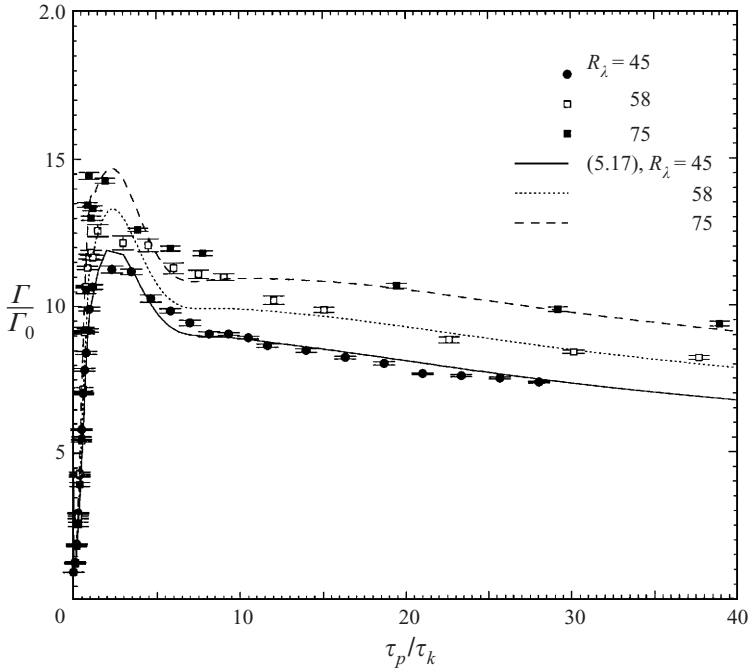

FIGURE 20. Comparison of the model prediction of the collision kernel with DNS data for different flow Reynolds numbers.

from 50 to 5000. The dimensionless collision kernel can be expressed as

$$\frac{\Gamma}{\Gamma_0} = 4.85\frac{\eta}{R}g(R)\frac{\langle|w_r|\rangle}{v_k}. \tag{5.17}$$

At low R_λ, there is only one maximum owing to the strong overlap between the turbulent transport effect and the accumulation effect, as seen in our DNS. At very high R_λ, the overlap is diminished as the separation between T_e and τ_k is increased. As a result, the turbulent transport effect shows up at $\tau_p \approx T_e$ while the accumulation effect is realized separately at $\tau_p \approx \tau_k$, yielding two evident peaks. There could also be a weak maximum point between these two main peaks owing to residual overlap effect, although this may be an artifact of the model.

Another observation is that the accumulation effect is much stronger than the turbulent transport effect at high Reynolds number. At $R_\lambda = 5000$, the first peak is about ten times the value of the second peak. At this Reynolds number, the collision kernel for particles with $\tau_p = \tau_k$ is about 700 times larger than that for fluid elements. The accumulation effect is dominant in, for example, collisions in clouds for particle sizes near $\tau_p \approx \tau_k$. Although the R_λ scaling of $g(R)$ requires further investigations, we believe that the above result is qualitatively correct.

To stress the importance of the accumulation effect further, we plot in figure 22 the modelled $g(R)$ as a function of τ_p/τ_k in a manner similar to figure 21. The value of $g(R)$ represents the difference between our model and the previous models that do not consider the accumulation effect (e.g. Williams & Crane 1983; Kruis & Kusters 1997). At $\tau_p/\tau_k = 1$, the accumulation effect causes an additional increase in the collision rate by a factor of 8, 71, and 701 for $R_\lambda = 50$, 500, and 5000, respectively. Furthermore, there is a finite-range of particle size with τ_p spanning τ_k for which the

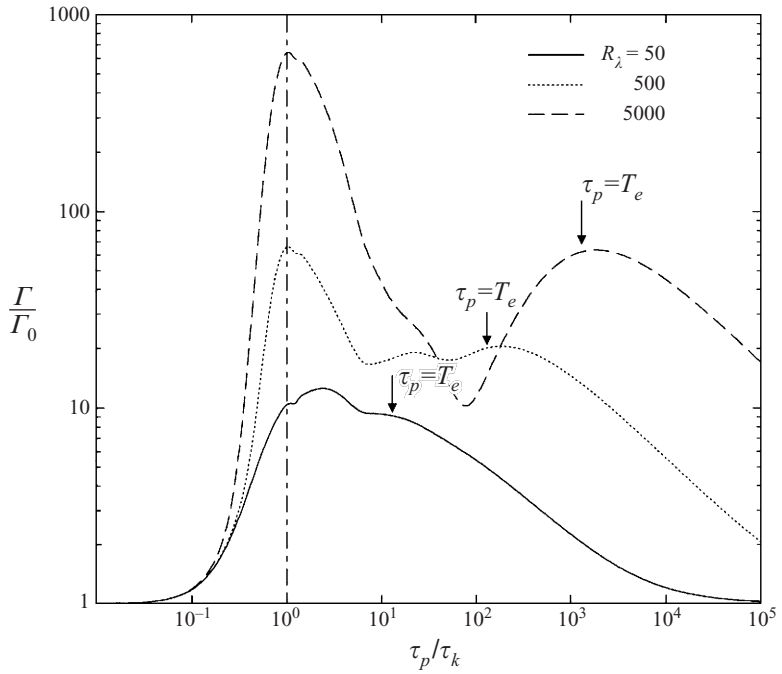

FIGURE 21. Model prediction of the collision kernel Γ/Γ_0 for high flow Reynolds numbers.

accumulation effect is significant. Therefore, it is crucial to include this effect in future modelling of turbulent coagulations.

6. Conclusions

We have conducted numerical experiments in order to advance our understanding of the collision rate of solid particles in a turbulent gas, extending the recent studies of Sundaram & Collins (1997) and Zhou *et al.* (1998). The collision rate is affected by two mechanisms, namely, turbulent fluctuations that cause relative motion between particles (the turbulent transport effect) and the preferential concentration that leads to a highly intermittent local pair density distribution and thus an additional enhancement to the average collision rate (the accumulation effect). The traditional formulation of the collision kernel by Saffman & Turner (1956) needs to be modified to include this accumulation effect for $\tau_p = O(\tau_k)$.

We have developed and validated the methodology to numerically separate the turbulent transport effect from the accumulation effect on the collision rate. This, along with DNS results of collision kernels, allows us to compare the spherical formulation and cylindrical formulation for finite-inertia particles, extending our recent work on the comparison of the two formulations for zero-inertia particles (Wang *et al.* 1998*b*). The accumulation effect is accounted for by the radial distribution function $g(R)$ at contact, which was first derived rigorously by Sundaram & Collins (1997). One assumption made by Sundaram & Collins (1997), that the probability density function of relative velocity is isotropic, however, renders their formulation equivalent to the cylindrical formulation. We found that the spherical formulation gave accurate prediction to the collision kernel for all τ_p/τ_k, as long as the concentration field had reached the statistically stationary stage. If the stationarity is not established,

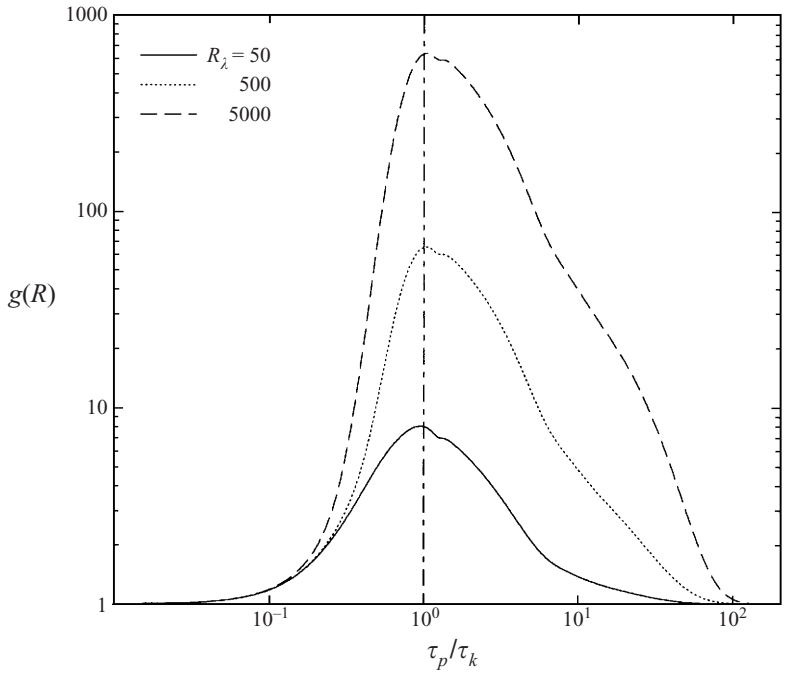

FIGURE 22. The modelled $g(R)$ as a function of τ_p/τ_k.

which may be the case in practical applications, a correction can be made to the spherical formulation in terms of the ratio of relative mass fluxes. We also found that the relative inward velocity can be 50% larger than the relative outward velocity when τ_p/τ_k is of the order of one. This is due to the probable negative velocity divergence in regions of high particle concentration (Maxey 1987).

The cylindrical formulation overpredicts the collision kernel for $\tau_p/\tau_k = O(1)$. The level of overprediction is largest for fluid elements (about 25%) but decreases quickly with particle inertia. The two formulations become identical for large particle inertia since interactions of particles with a wide range of random eddies remove the orientational dependence of the relative velocity on pair separation vector. Probability density functions, variance, and asymmetry of the relative velocity have all been quantified in both the radial and transverse directions to further corroborate the above finding.

We have quantified the turbulent transport effect and the accumulation effect for a full range of particle inertia and several flow Reynolds numbers. For fully developed turbulence, the turbulent transport effect can lead to an increase of inter-particle collision rate by a factor of as much as u'/v_k, relative to the collision rate of fluid elements. Therefore, the maximum level of the turbulent transport effect scales with $R_\lambda^{1/2}$ (Hinze 1975). Various analytical models for the pair relative velocity are compared to simulation results. A working model is proposed for the turbulent transport effect as a function of R_λ and τ_p/τ_k.

The accumulation effect is strongest when $\tau_p/\tau_k = 1$, in accordance with the Kolmogorov scaling for particle concentration first discovered by Wang & Maxey (1993). Within a rather limited range of flow Reynolds number, we found that the accumulation effect scales linearly with flow Reynolds number. A qualitative explanation is that the level of intermittency of the vortical structures increases with

flow Reynolds number and thus the level of particle accumulation. The maximum increase in the collision rate due to the accumulation effect is around $(1 + 0.14R_\lambda)$, relative to the collision rate in a random suspension. Furthermore, we have devised an empirical expression to describe the accumulation effect in terms of the relative particle inertia. An analytical model for the accumulation effect based on vortex tube structure is needed and should be explored in the future.

Finally, an integrated working model for predicting the collision kernel in terms of flow Reynolds number and particle inertia has been proposed. This model suggests that while at low Reynolds number, there is a peak collision kernel at intermediate particle inertia ($\tau_k < \tau_p < T_e$) owing to the overlap of the turbulent transport effect and the accumulation effect; there can be multiple peaks at large flow Reynolds number. The first peak, which is most pronounced, occurs at $\tau_p/\tau_k = 1$, owing to the accumulation effect. A secondary peak occurs at $\tau_p/T_e = 1$, owing to the dominant contribution of the turbulent transport effect. There may also be a weak, third peak at intermediate inertia, owing to the overlapping of the two effects. Such a model is essential for modelling particle size distribution in turbulent suspension using population balance equations (e.g. Pruppacher & Klett 1978). It is also useful for numerical modelling of particle–particle collisions using large–eddy simulation approach (Gourdel, Simonin & Brunier 1998).

The strong dependence of the collision rate on Reynolds number when $\tau_p/\tau_k = \mathcal{O}(1)$ has an important application to the modelling of cloud microphysics. The average dissipation rate $\bar{\epsilon}$ can range from about $10\,\mathrm{cm^2\,s^{-3}}$ for stratiform clouds, $100\,\mathrm{cm^2\,s^{-3}}$ for small cumulus clouds, and up to $2500\,\mathrm{cm^2\,s^{-3}}$ in very strong cumulus congestus (Ackerman 1967; Panchev 1971; Weil, Lawson & Rodi 1993). Therefore, droplets in the size range from 10 to 200 μm could have an inertial response time of the order of the flow Kolmogorov time. The Taylor microscale Reynolds number in the clouds is of the order of 10^3 to 10^4. Therefore, the accumulation effect can lead to 100 to 1000 times increase in the collision rate. This may help explain the rapid growth of droplets in size ranges where neither condensation nor differential gravitational settling is effective.

Although this paper is restricted to monodisperse systems, the methods can be easily extended to polydisperse systems. These results are being collected and will be presented in a subsequent paper.

This work was supported by the University of Delaware Research Foundation, the IBM Watson Research Center, and the State of Delaware. L-.P. W. is grateful to Professors Lance Collins and Martin Maxey for several helpful discussions in the course of this work. Specifically, insightful discussions with Professor Collins motivated our careful investigations on the turbulent transport effect and the accumulation effect. The direct numerical simulations were performed on the SGI Power Challenge supercomputer at the University of Delaware.

REFERENCES

Abrahamson, J. 1975 Collision rates of small particles in a vigorously turbulent fluid. *Chem. Engng Sci.* **30**, 1371–1379.

Ackerman, B. 1967 The nature of the meteorological fluctuations in clouds. *J. Applied Met.* **6**, 61–71.

Allen, M. P. & Tildesley, D. J. 1987 *Computer Simulation of Liquids*. Oxford University Press.

Anselmet, E., Gagne, Y., Hopfinger, E. J. & Antonia, R. A. 1984 High-order velocity structure functions in turbulent shear flows. *J. Fluid Mech.* **140**, 63–89.

de Boer, G. B. J., Hoedemakers, G. F. M. & Thoenes, D. 1989 Coagulation in turbulent flow: Part I and Part II. *Chem. Engng Res. Des.* **67**, 301–307 and 308–315.

Brunk, B. K., Koch, D. L. & Lion, L. W. 1997 Hydrodynamic pair diffusion in isotropic random velocity fields with application to turbulent coagulation. *Phys. Fluids* **9**, 2670–2691.

Brunk, B. K., Koch, D. L. & Lion, L. W. 1998*a* Turbulent coagulation of colloidal particles. *J. Fluid Mech.* **364**, 81–113.

Brunk, B. K., Koch, D. L. & Lion, L. W. 1998*b* Observations of coagulation in isotropic turbulence. *J. Fluid Mech.* **371**, 81–107.

Delichatsios, M. A. 1980 Particle coagulation in steady turbulent flows: application to smoke aging. *J. Colloid Interface Sci.* **78**, 163–174.

Delichatsios, M. A. & Probstein, R. F. 1975 Coagulation in turbulent flow: Theory and experiment. *J. Colloid Interface Sci.* **51**, 394–405.

Elghobashi, S. 1994 On predicting particle-laden turbulent flows. *Appl. Sci. Res.* **52**, 309–329.

Fessler, J. R., Kulick, J. D. & Eaton, J. K. 1994 Preferential concentration of heavy particles in a turbulent channel flow. *Phys. Fluids* A **6**, 3742–3749.

Flagan, R. C. & Seinfeld, J. H. 1988 *Fundamentals of Air Pollution Engineering*. Prentice Hall, Englewood Cliffs.

Gourdel, C., Simonin, O. & Brunier, E. 1998 Modeling and simulation of gas–solid turbulent flows with a binary mixture of particles. *Third International Conference on Multiphase Flow*, 8–12 June, Lyon, France. CD-ROM publication (paper 504).

Higashitani, K., Yamauchi, K., Matsuno, Y. & Hosokawa, G. 1983 Turbulent coagulation of particles dispersed in a viscous fluid. *J. Chem. Engng Japan* **16**, 299–304.

Hinze, J. O. 1975 *Turbulence*, pp. 175–250. McGraw-Hill.

Hu, C. & Mei, R. 1997 Effect of inertia on the particle collision coefficient in Gaussian turbulence. *The 7th Intl Symp. on Gas–Solid Flows*, Paper FEDSM97-3608, ASME Fluids Engineering Conference, Vancouver, BC, Canada.

Jimenez, J., Wray, A. A., Saffman, P. G. & Rogallo, R. S. 1993 The structure of intense vorticity in isotropic turbulence. *J. Fluid Mech.* **255**, 65–90.

Jonas, P. R. & Goldsmith, P. 1972 The collection efficiencies of small droplets falling through a sheared air flow. *J. Fluid Mech.* **52**, 593–608.

Khain, A. P. & Pinsky, M. B. 1995 Drop inertia and its contribution to turbulent coalescence in convective clouds. Part I. Drop fall in the fall with random horizontal velocity. *J. Atmos. Sci.* **52**, 196–206.

Koziol, A. S. & Leighton, H. G. 1996 Turbulent particle dispersion: a comparison between Lagrangian and Eulerian modeling approaches. *J. Atmos. Sci.* **53**, 1910–1920.

Kruis, F. E. & Kusters, K. A. 1997 The collision rate of particles in turbulent flow. *Chem. Engng Comm.* **158**, 201–230.

Kuboi, R., Komasawa, I. & Otake, T. 1972 Collision and coalescence of dispersed drops in turbulent liquid flow. *J. Chem. Engng Japan* **5**, 423–424.

Lichtenfeld, H., Knapschinsky, L., Sonntag, H. & Shilov, V. 1995 Fast coagulation of nearly spherical ferric oxide (haematite) particles. *Colloids Surface* A **104**, 313–320.

Maxey, M. R. 1987 The gravitational settling of aerosol particles in homogeneous turbulence and random flow fields. *J. Fluid Mech.* **174**, 441–465.

Maxey, M. R. & Riley, J. J. 1983 Equation of motion for a small rigid sphere in a nonuniform flow. *Phys. Fluids* **26**, 883–889.

O'Rourke, P. J. & Bracco, F. V. 1980 Modelling of drop interactions in thick sprays and a comparison with experiments. *Stratified Charge Automotive Engines Conference*, The Institution of Mechanical Engineers, London, p. 101.

Panchev, S. 1971 *Random Function and Turbulence*, pp. 301–309. Pergamon.

Pinsky, M. B. & Khain, A. P. 1994 Initiation of drop velocity oscillations during their fall in a vertically sheared flow with embedded velocity fluctuation. *Geophys. Astrophys. Fluid Dyn.* **78**, 169–192.

Pruppacher, H. R. & Klett, J. D. 1978 *Microphysics of Clouds and Precipitation.* D. Reidel.

Reade, W. C. & Collins, L. R. 1998 Effect of preferential concentration on turbulent collision rates. *Phys. Fluids* (submitted).

Reuter, G. W., Villiers, R. de & Yavin, Y. 1988 The collection kernel for two falling cloud drops

subjected to random perturbations at a turbulent airflow: A stochastic model. *J. Atmos. Sci.* **45**, 765–773.

Saffman, P. G. & Turner, J. S. 1956 On the collision of drops in turbulent clouds. *J. Fluid Mech.* **1**, 16–30; also Corrigendum 1988, **196**, 599.

Squires, K. D. & Eaton, J. K. 1991 Preferential concentration of particles by turbulence. *Phys. Fluids* A **3**, 1169–1179.

Sundaram, S. & Collins, L. R. 1996 Numerical considerations in simulating a turbulent suspension of finite-volume particles. *J. Comput. Phys.* **124**, 337–350.

Sundaram, S. & Collins, L. R. 1997 Collision statistics in an isotropic, particle-laden turbulent suspension. *J. Fluid Mech.* **335**, 75–109.

Tang, Y. & Lu, B. C.-Y. 1995 Improved expressions for the radial distribution function of hard spheres. *J. Chem. Phys.* **103**, 7463–7470.

Tang, Y. & Lu, B. C.-Y. 1997 Analytical representation of the radial distribution function for classical fluids. *Mol. Phys.* **90**, 215–224.

Vincent, A. & Meneguzzi, M. 1991 The spatial structure and statistical properties of homogeneous turbulence. *J. Fluid Mech.* **225**, 1–20.

Wang, L.-P., Chen, S., Brasseur, J. G. & Wyngaard, J. C. 1996 Examination of hypothesis in the Kolmogorov refined turbulence theory through high-resolution simulations. Part 1. Velocity field. *J. Fluid Mech.* **309**, 113–156.

Wang, L.-P. & Maxey, M. R. 1993 Settling velocity and concentration distribution of heavy particles in homogeneous isotropic turbulence. *J. Fluid Mech.* **256**, 27–68.

Wang, L.-P., Wexler, A. S. & Zhou, Y. 1998*a* On the collision rate of small particles in isotropic turbulence. Part 1. Zero-inertia case. *Phys. Fluids* **10**, 266–276.

Wang, L.-P., Wexler, A. S. & Zhou, Y. 1998*b* Statistical mechanical descriptions of turbulent coagulation. *Phys. Fluids* **10**, 2647–2651.

Weil, J. C., Lawson, R. P. & Rodi, A. R. 1993 Relative dispersion of ice crystal in seeded cumuli. *J. Appl. Met.* **32**, 1055–1072.

Williams, J. J. E. & Crane, R. I. 1979 Drop coagulation in cross-over pipe flows of wet steam. *J. Mech. Engng Sci.* **21**, 357–360.

Williams, J. J. E. & Crane, R. I. 1983 Particle collision rate in turbulent flow. *Intl J. Multiphase Flow* **9**, 421–435.

Xiong, Y. & Pratsinis, S. 1991 Gas phase production of particles in reactive turbulent flows. *J. Aerosol Sci.* **22**, 637–655.

Yuu, S. 1984 Collision rate of small particles in a homogeneous and isotropic turbulence. *AIChE J.* **30**, 802–807.

Zhou, Y., Wexler, A. S. & Wang, L.-P. 1998 On the collision rate of small particles in isotropic turbulence. Part 2: Finite inertia case. *Phys. Fluids* **10**, 1206–1216.

Zinchenko, A. Z. & Davis, R. H. 1995 Collision rates of spherical drops or particles in a shear flow at arbitrary Péclet number. *Phys. Fluids* **7**, 2310–2327.